### **HIGHLIGHT**

# Recent Advances in Microfluidics Enabled Controlled Reaction, Assembly and Exfoliation of Inorganic Nanomaterials

V. Vinay K. Doddapaneni<sup>a</sup>, Alvin Chang<sup>b</sup>, Ho-Young Jun<sup>c</sup>, Chang-Ho Choi<sup>c\*</sup>, Zhenxing Feng<sup>a</sup>, Chih-Hung Chang<sup>a\*</sup>

Received 00th January 20xx, Accepted 00th January 20xx

DOI: 10.1039/x0xx00000x

Microfluidics, involving chemical or physical phenomena in the order of submillimeter length scale under continuous flow, allows controlled reaction, assembly, and exfoliation of nanomaterials by adjusting momentum, heat, and mass transfer. This highlight explores recent progress in studies demonstrating the ability to control reaction and assembly for various inorganic nanomaterials, including metal, metal chalcogenide, metal oxide, composite and doped nanomaterials, and two-dimensional nanosheets in microfluidics, with representative case studies of each type of material. Furthermore, this highlight discusses the current challenges and gaps in the field of controlled reaction, assembly, and exfoliation of nanomaterials in microfluidics and future research directions.

#### 1. Introduction

Nanomaterials have recently attracted applications in diverse fields such as medicine, electronics, sensing, energy storage, energy harvesting, catalysis, and many others because of their distinctive properties compared to their bulk counterparts. 1-3 Taking advantage of the unique properties that arise from the nanoscale regime, numerous efforts have been made to investigate innovative ways to tailor nanomaterial properties by tuning their size, shape, and composition to improve their performance for specific targeted applications.4 For example, anisotropic nanomaterials such as nanorods, nanotubes, and linear assembly of nanomaterials have better performance than spherical nanoparticles in magnetic resonance imaging applications.<sup>5,6</sup> Localized surface plasmon resonance (LPSR) effect of metal nanoparticles such as Ag, Au, and Cu and the non-linear optical properties of nanomaterials is heavily influenced by the size of nanoparticles. It thereby influences the efficiency of the processes they are being used for.<sup>7–9</sup> The power conversion efficiency (PCE) of perovskite solar cells incorporated with Au nanoparticles has increased from 14.60% to 16.20% when the diameter is decreased from 70 nm to 30 nm.8 Nature-inspired nanostructures have also been proven to improve the efficacy of the processes in renewable energy applications such as solar cells, optoelectronics, photocatalysis, rechargeable batteries, contact angle modification, and spilled oil collection. 10,11 Modifying these morphologies, dimensions, and composition is possible by precisely controlling the reaction mechanism during the synthesis process and assembly of the nanomaterials.

Various top-down (mechanical milling, photolithography, etching, laser ablation, sputtering, high-sheer mixing exfoliation,

hall-mill assisted exfoliation, electrochemical exfoliation, solvothermal-assisted liquid phase exfoliation, SALPE) and bottomup (hydro/solvothermal, sol-gel, polyol, biological, supercritical fluid synthesis, microemulsion, chemical vapor deposition, spray pyrolysis) approaches are developed to synthesize nanomaterials (Fig. 1a) for a wide variety of applications.<sup>4,12-15</sup> Of all these techniques, solution-based processes offer the advantages of high throughput and relatively simple equipment over vapor-based techniques. 16 A vast library of nanomaterials has been synthesized using these both bottom-up and top-down solution-based synthesis techniques, such as metals (Ag, Au, Bi, Co, Cu, Fe, Ni, Pd, Pt, Rh), metal oxides (CdO, CeO<sub>2</sub>, Co<sub>3</sub>O<sub>4</sub>, CuO, Er<sub>2</sub>O<sub>3</sub>, Fe<sub>2</sub>O<sub>3</sub>, Mn<sub>3</sub>O<sub>4</sub>, TiO<sub>2</sub>, SmVO<sub>4</sub>, SnO<sub>2</sub>, WO<sub>X</sub>, ZnO), nanocomposites (hexagonal boron nitride/titania), chalcogenides (Ag<sub>8</sub>SnS<sub>6</sub>, CdSe, Cu<sub>x</sub>S) and twodimensional nanosheets (black phosphorous, graphene). 15,17-25 Some of the selected recent works with the controlled synthesis of nanomaterials using batch methods are listed in Table 1. Nonetheless, in a batch-scale bottom-up synthesis approach, the growth and nucleation of nanomaterials is still a complex mechanism to generalize one phenomenon to all classes of nanomaterials. However, from the extensive investigations, the governing process to tune the morphologies, size, shape, and composition of nanomaterials is dependent on integrated effects of reaction rate, temperature, concentration, mixing of reactants, residence time, solvents, and the additives such as reducing agents, pH modifiers involved in the process.  $^{4,12,13,18-20,23,26,27}$ 

Electronic Supplementary Information (ESI) available: [details of any supplementary information available should be included here]. See DOI: 10.1039/x0xx00000x

<sup>&</sup>lt;sup>a</sup> School of Chemical, Biological and Environmental Engineering, Oregon State University, Corvallis, OR, USA 97331. E-mail: Chih-hung.chang@oregonstate.edu
<sup>b</sup> School of Mechanical, Industrial and Manufacturing Engineering, Oregon State University, Corvallis, OR, USA 97331.

<sup>&</sup>lt;sup>c</sup> Department of Chemical Engineering, Gyeongsang National University, Jinjudaero 501, Jinju-si, Gyeongsangnam-do, South Korea 52828. E-mail: ch\_choi@gnu.ac.kr † Footnotes relating to the title and/or authors should appear here.

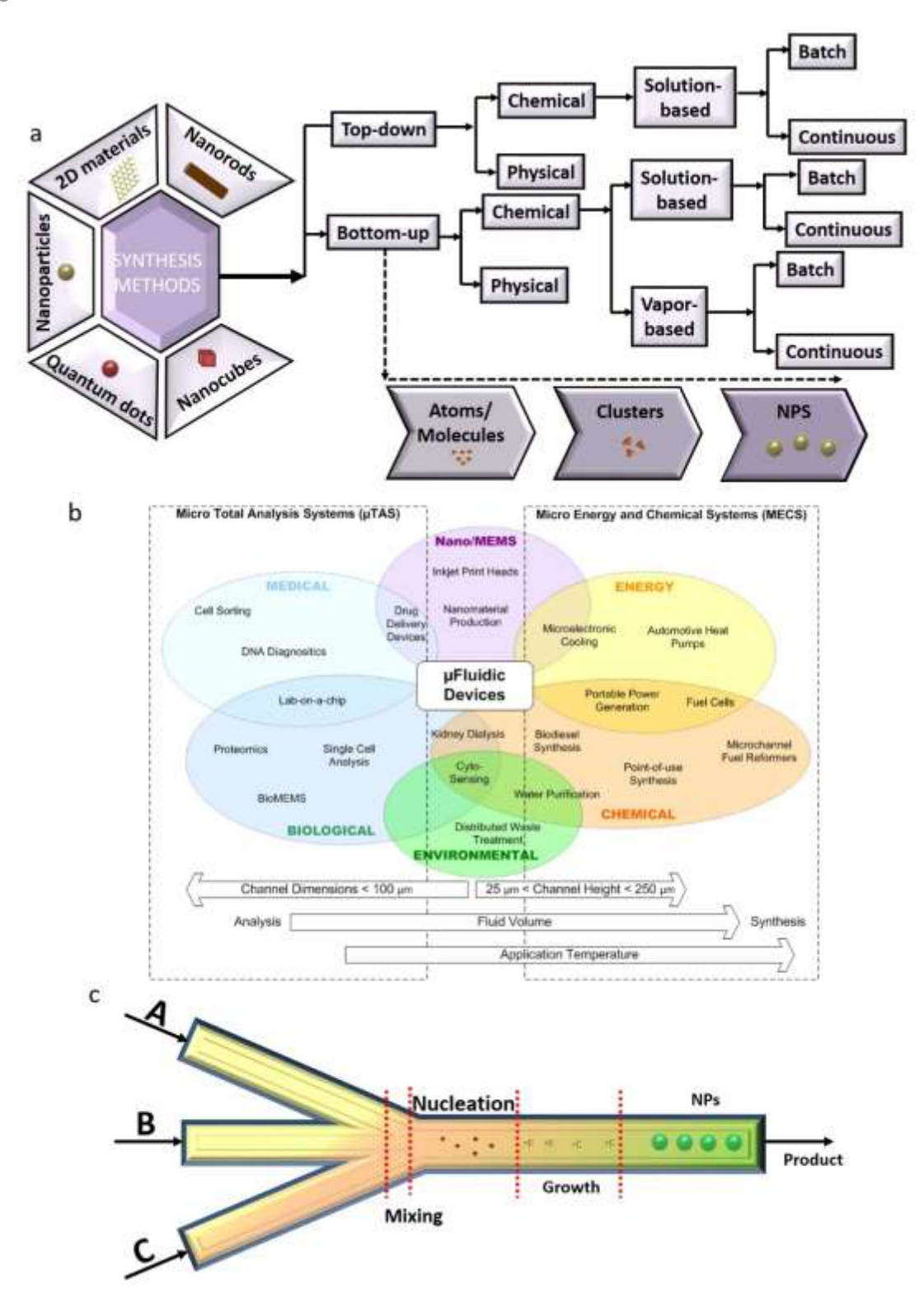


Fig. 1 (a) Different types of nanomaterials and synthesis methods, (b) diverse applications of microfluidics (reproduced with permission from 54: copyright 2008, Springer, (c) microfluidic reactor.

Table 1 Recently published works on different types of nanomaterials produced by batch synthesis

| Material   | Strategy  | Synthetic Method   | Features    | Reference |
|--|-----------|--------------------|-------------|-----------|
| Ag Nanowires (NWs)   | Bottom-up | Polyol             | 50-70 nm    | 28        |
| Au   | Bottom-up | Chemical reduction | 6-22 nm     | 29        |
| BP nanosheets  | Top-down  | Electrochemical    | 0.5-30 μm   | 30        |
| BP nanosheets  | Bottom-up | Solvothermal       | 4.7 nm      | 31        |
| BP nanosheets  | Bottom-up | Solvothermal       | 1-15 nm     | 32        |
| BaTiO₃   | Bottom-up | Solvothermal       | 10 nm       | 33        |
| BaTiS₃ nanorods  | Bottom-up | Hot-injection      | 50 nm       | 34        |
| CoFe <sub>2</sub> O <sub>4</sub>   | Bottom-up | Solvothermal       | 7-10 nm     | 35        |
| CoSnO₃ cubes   | Bottom-up | Hydrothermal       | 250 nm      | 36        |
| CuS Nanorods   | Bottom-up | Microwave          | -           | 37        |
| Fe <sub>3</sub> O <sub>4</sub> @SiO <sub>2</sub> core-shell  | Bottom-up | Emulsion           | 76-152 nm   | 38        |
| Graphene nanosheets  | Top-down  | Ball-milling       | -           | 39        |
| Graphene nanosheets  | Top-down  | Electrochemical    | 100-500 nm  | 40        |
| Graphene nanosheets  | Top-down  | High-shear         | 160 nm      | 41        |
| Graphene nanosheets  | Top-down  | SALPE              | 100-800 nm  | 42        |
| Graphene nanosheets  | Top-down  | Ultrasound induced | 100-500 nm  | 43        |
| h-BN nanosheets  | Top-down  | Ball-milling       | 1.5-2 μm    | 44        |
| Li-boron oxide nanocomposites  | Bottom-up | Sol-gel            | 20-50 nm    | 45        |
| Li <sub>4</sub> Zn <sub>3</sub> B <sub>4</sub> O <sub>11</sub> /Li <sub>2</sub> B <sub>2</sub> O <sub>4</sub> nanocomposites | Bottom-up | Sol-gel            | 22-135 nm   | 46        |
| M <sub>O</sub> S <sub>2</sub> nanosheets   | Top-down  | SALPE              | 40 nm       | 47        |
| MoS <sub>2</sub> nanoflakes  | Bottom-up | Hydrothermal       | 30-50 nm    | 27        |
| Pb chalcogenides   | Bottom-up | Hot-injection      | 1.6-12.1 nm | 48        |
| Pd   | Bottom-up | microemulsion      | 2-9 nm      | 49        |
| PdCu on rGO  | Bottom-up | solvothermal       | 3.8-4.6 nm  | 50        |
| Pd₂N nanocubes   | Bottom-up | Hydrothermal       | 18 nm       | 51        |
| Lotus-ZnO decorated graphene oxide   | Bottom-up | Sol-gel            | -           | 52        |

While in a batch scale top-down exfoliation method, low exfoliation efficiency, inconsistent driving force leading to inconsistent dimensions of the nanosheets, and longer exfoliation times are major concerns. 15,53

Despite the tremendous progress in manufacturing various morphologies, sizes, shapes, and compositions of nanomaterials using batch methods at the lab scale, experimental control over the parameters is difficult at large-scale. Microfluidics overcomes this barrier by providing exceptional control over the parameters via the process intensification approach at the microscale. It enables the controlled reaction, assembly, and exfoliation of nanomaterials for targeted applications and continuous nanomanufacturing at a point of use. Since their inception, microfluidics expanded from microanalytical methods to field deployable sensors, cell analysis, microelectronics, chemical synthesis, nanomaterial production, energy storage, printing, and many other applications, as shown in Fig. 1 b.54-57 Particularly, the field of nanomaterial synthesis and production is revolutionized by microfluidics channel dimensions (tens to hundreds of microns) and their ability to handle small amounts of fluids, leading to reduced material wastage over conventional flask reactors. They have advantages in scaling up by the "numbering-up" approach with stacks of single microreactors (Fig. 1c) in parallel, providing the same process intensification over

scaling up from a small flask reactor to a large-scale batch reactor.  $^{54,58}$ 

This highlight article attempts to communicate the recent progress and prospects in controlled reaction, assembly, and exfoliation of nanomaterials possible by fine-tuning transport processes at the microscale using microfluidics. A brief discussion about the momentum, heat, and mass transfer control at the microscale is presented in the following section, along with case studies of the aspects mentioned above to highlight the influence of the reaction, assembly, and exfoliation of different nanomaterials categorized into metals, metal oxides, chalcogenides composite and doped nanomaterials, and 2D-nanosheets.

### **2.** Types of microfluidics for nanomaterial synthesis Bottom-up microfluidics approach

Microfluidics for nanomaterial synthesis can be mainly categorized into tubular microreactors and lab-on-chip types, as shown in Fig. 2 a & b. Tubular microreactors <sup>59</sup> are typically made of plastic, glass, or stainless-steel tubes; these are free-standing and connected to a pumping system on the one end; nanomaterials are collected on the other. The material choice for the reactors depends on the type of chemicals, chemistry, and reaction temperature. The precursor streams going through the reactor may be subjected to different thermal zones usually maintained by an oil bath. On the other hand,

lab-on-chip devices  $^{60}$  are usually microchannels supported by a base material. Micro heating elements and localized heating methods can heat these reactors.

#### Top-down microfluidics approach

Furthermore, there is a particular case of micro fluidization methods for producing 2D nanosheets. Microfluidization, acoustic microfluidics (AM), wet-jet milling (WJM), and lab-on-chip. 61–66 The characteristics of each microfluidic method is briefly introduced below.

**Microfluidization.** This high-pressure homogenization technology is applied to produce nanoemulsions in the pharmaceutical and food industries. A typical microfluidization system consists of an intensifying pump, an interaction chamber, and a cooling chamber, as shown in Fig. 2c. A high-pressure intensifying pump delivers a bulk 2D material dispersion to the interaction chamber at constant pressure. Z-shaped microchannels within the interaction chamber are critical for generating high shear rates and homogenizing high shear rates in the dispersion. At these high shear forces, bulk 2D materials are subject to rapid fragmentation and exfoliation, producing 2D nanosheets (Fig. 2d). After exfoliation in the interaction chamber, the dispersion containing 2D nanosheets is cooled in a cooling jacket to protect 2D nanosheets from defect formation.

Wet-jet milling (WJM). WJM consists of a pneumatic valve, piston, processor, and chiller (Fig. 2e). Its configuration and exfoliation mechanism are similar to those of microfluidization. A pneumatic valve and piston create high pressure to deliver the 2D bulk materials dispersion to the interconnected disk. Unlike microfluidization, in which strong shear occurs in the Z-shaped microchannel, wet-jet milling utilizes a high shear force created at the micronozzle that 2D material dispersion is instantaneously encountered in the interconnected disk. Following exfoliation in the micronozzle, the dispersion containing 2D nanosheets is sent to a chiller to prevent the defect formation of 2D nanosheets.

Acoustic-microfluidic (AM). AM process is similar to conventional LPE in a sonication bath; instead of having a batch container such as a vial and a beaker, the process equips with microfluidic capillary tubing (Fig. 2f) in this process. The simplicity of using a sonic bath combines the inherent advantages of microfluidics, offering the AM process as a cost-effective and rapid production platform to produce 2D nanosheets. Particularly, bulk 2D material dispersion is forced to flow during the exfoliation process and thus prevents the settlement of bulk 2D materials, leading to high exfoliation efficiency. Optimizing the flow rate also enhances the exfoliation efficiency by promoting the cavitation effect.

Lab-on-chip process. This process exploits hydrodynamic cavitation to exfoliate 2D nanosheets. The dynamic pressure is generated and increased as bulk 2D material dispersion passes through the micro gap inside the chip (Fig. 2g). The hydrodynamic cavitation becomes effective downstream in the chip, where bubbles start to collapse caused by recovering the initial flow rate of the dispersion. By repeating the exfoliation process thousands of times, 2D nanosheets

can be obtained. The Lab on chip process can benefit from a low-power operation but requires a highly extended processing time.

# 3. Diverse methods of regulating transport phenomenon in microfluidics

Chemical reactions depend on the reactant's concentration and distribution of reactant concentration, temperature, temperature distribution, and reaction time and distribution. The transport processes can impact all these factors via momentum, heat, and mass transfer. By governing these transport processes, one can control the chemical reaction. As discussed in the above section, microfluidics with the capability of intensifying these transport processes is among of most significant interest for next-generation nanomanufacturing. The following paragraphs dive into the different routes to control the transport processes to achieve the desired results in manufactured nanomaterials.

The ability of fluids to transport momentum via viscosity is critical for microfluidics design. Momentum transport can be thought of as frictional force in the fluid in which an external force felt by one layer of the fluid drags adjacent fluid layers along. Momentum transport governs the fluid's flow and impacts the flow's velocity and behavior. The most basic and advantageous capability of microfluidics over the conventional batch reactor systems is their ability to adjust fluid flow rates, thereby precisely controlling the concentration ratios of each reactant and other additives that are needed for the reaction and the capability to introduce the reactants at the required zone in the reactor spatially to precisely dictate the nanoparticle's size, shape, and composition. The residence time of reactants, intermediary species, nanoclusters, and nanoparticles inside the reactor can be varied precisely by adjusting the flow rates and flow behavior. Flow control within microfluidics is possible from simple syringe pumps by either passive or active flow control.67

One common flow control application is for droplet-based microfluidics, which aims to create a tunable stream of droplets in the hundreds of nanometer to micrometer range. These devices are advantageous due to the small volume of reagents required, controllable and uniform production of droplets, and high surfacearea-to-volume ratios. Droplet generation can be obtained by either passive or active control techniques (Fig. 3a).<sup>68</sup> Passive flow control techniques require no external energy input into the system and instead rely on the shaping and architecture of the microfluidic device itself. An example of passive flow control is illustrated in Fig. 3b, which outlines the design of a microsphere generation device known as the flow focusing and T-junction (FF-TJ) device.<sup>69</sup> It operates using the principles of flow focusing and a T-junction, which relies on using two fluids, the outside continuous flow liquid, and the inside dispersed flow liquid. The continuous flow disrupts the dispersed flow liquid and creates shear stress to separate the dispersed liquid and generate droplets. In the first section of the device, flow focusing is produced by using two liquids of different flow rates, where the outer liquid (the sheath flow) has a higher velocity than the inner liquid (the middle flow) and thus decreases the diameter and increases the shear stress in the central flow. The second section of the device uses a T-junction in which the primary

channel fluid hits the side channel fluid at the "T-junction", creating shear stress in the dispersed flow and creating droplets. Although flow focusing produces microspheres, in the FF-TJ, the purpose of the flow focusing segment is to adjust the size of the middle flow by

varying the flow ratio between the inner and outer liquids to control microsphere size.<sup>69</sup> Other passive microsphere generation methods exist, such as T-junctions and flow-focusing devices by themselves and microemulsion techniques<sup>67</sup> and another form of flow behavior

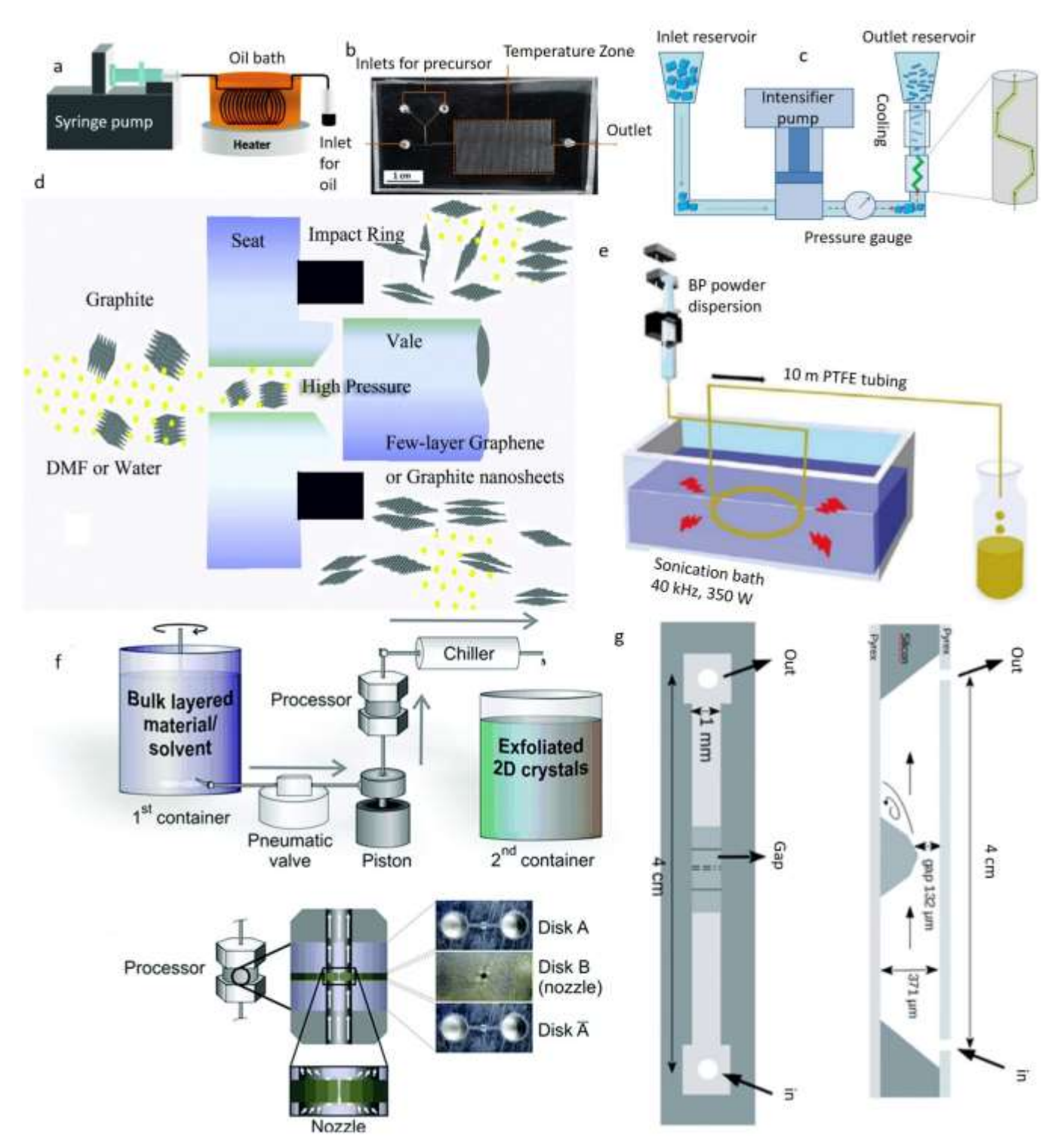


Fig. 2 Schematics of (a) tubular microreactor (reproduced with permission from<sup>59</sup>: copyright 2004, American Chemical Society), (b) lab-on-chip for nanomaterials(reproduced with permission from<sup>60</sup>: under the terms of CC BY 4.0, http://creativecommons.org/licenses/by/4.0/) (c) microfluidization (reproduced with permission from<sup>62</sup>: copyright 2017, American Chemical Society, CC-BY 4.0, https://pubs.acs.org/page/policy/authorchoice\_ccby\_termsofuse.html), (d) high pressure homogenizer (reproduced with permission from<sup>63</sup>: copyright 2015, Royal Society of Chemistry), (e) acoustic-microfluidics nanosheets (reproduced with permission from<sup>64</sup>: copyright 2017, Elsevier), (f) wet-jet milling homogenizer (reproduced with permission from<sup>65</sup>: copyright 2018, Royal Society of Chemistry), and (g) lab-on chip used to produce 2D nanosheets (reproduced with permission from<sup>66</sup>: under the terms of CC BY-NC 3.0, https://creativecommons.org/licenses/by-nc/3.0/).

that can be achieved in microfluidic devices includes spiral flow created by slanted grooves on the capillary walls.

Unlike passive flow control devices, active flow control uses an outside energy source to drive and regulate changes in flow rate and behavior. An example of active flow control is summarized in Fig. 4a, in which a hydrogel valve is magnetically controlled to regulate the flow.  $^{70}$  It takes advantage of a temperature-responsive hydrogel that can swell and collapse efficiently on small scales. The hydrogel wells and closes the valve when the temperature is below the lower critical solution temperature (LCST). The hydrogel encases  $Fe_3O_4$  nanoparticles which heat upon application of an alternating magnetic field (AMF) and can bring the hydrogel above the LCST. Toggling the area on and off can control the state of the hydrogel and thus dictate the flow of the fluid.  $^{70}$  Other methods to externally actuate flow exist, and further examples of active flow control include pneumatically controlled centrifugal microfluidic devices  $^{71}$  and electrochemically toggled microvalves  $^{72}$ .

Another significant factor is mixing reactants and additives inside the reactor to enhance the mass transfer and provide optimum conditions for the reaction. Unlike macro-scale reactors, the mixing in the micro-scale reactors is not by turbulent mixing but rather by diffusion because of the low Reynolds number (Re) and laminar flow conditions at the micro-scale. As diffusion-based mixing is often time-inefficient, this is a well-known problem in microfluidics, and many active and passive methods have been developed to address this problem. As such, flow control is also integrated with mass transfer to improve the mixing conditions and enhance the mass transfer during the reaction process. Several active and passive mixing strategies, including grooves in the fluid path, segmented

flows, multi-laminating, spiral channels, collision of jets, Y or T type flow, dean vortices, and external fields such as light, electric fields, ultrasound and acoustics have been used to enhance the mixing and, thereby, mass transfer.<sup>73</sup>

One passive mixing strategy is through the use of droplet-based mixing. In this setup, a Y-junction and flow-focusing design was used to shear the continuous biphasic phase of PEGDA and fluorescent PEGDA (Fig. 4b).<sup>74</sup> As shown by fluorescent imaging, initially, the two reagents experience little cross-mixing within the droplet due to two symmetric recirculation zones. The two liquids are shown as two unmixed halves. Droplets are pushed out towards the outer edges of the capillary and then rotated due to the nonuniform flow field, leading to a uniform and well-mixed droplet.<sup>62</sup> Other examples of passive-based designs use micropillars and micronozzles<sup>75</sup>, finshaped baffles<sup>76</sup>, and spiral microchannels<sup>77</sup> to enhance mixing efficiency.

Active mixing strategies rely on an external stimulus to induce mixing and can achieve more flexible and tunable mixing at the cost of increased complexity. **Error! Reference source not found.**a illustrates the design of a micromixer which can be optically actuated. The device consists of three phases, two oil phases and one photosensitive aqueous phase with AzoTAB surfactant separating the oil phases. When not triggered, the aqueous phase is a continuous stream, preventing the mixing of the two oil phases. However, once a UV stimulus is applied, the aqueous phase forms into microdroplets, allowing the two oil phases to touch and mix with various efficiencies depending on the chamber position. Upon the removal of UV light, the droplets return to a continuous flow, demonstrating reversible mixing of the oil phases.

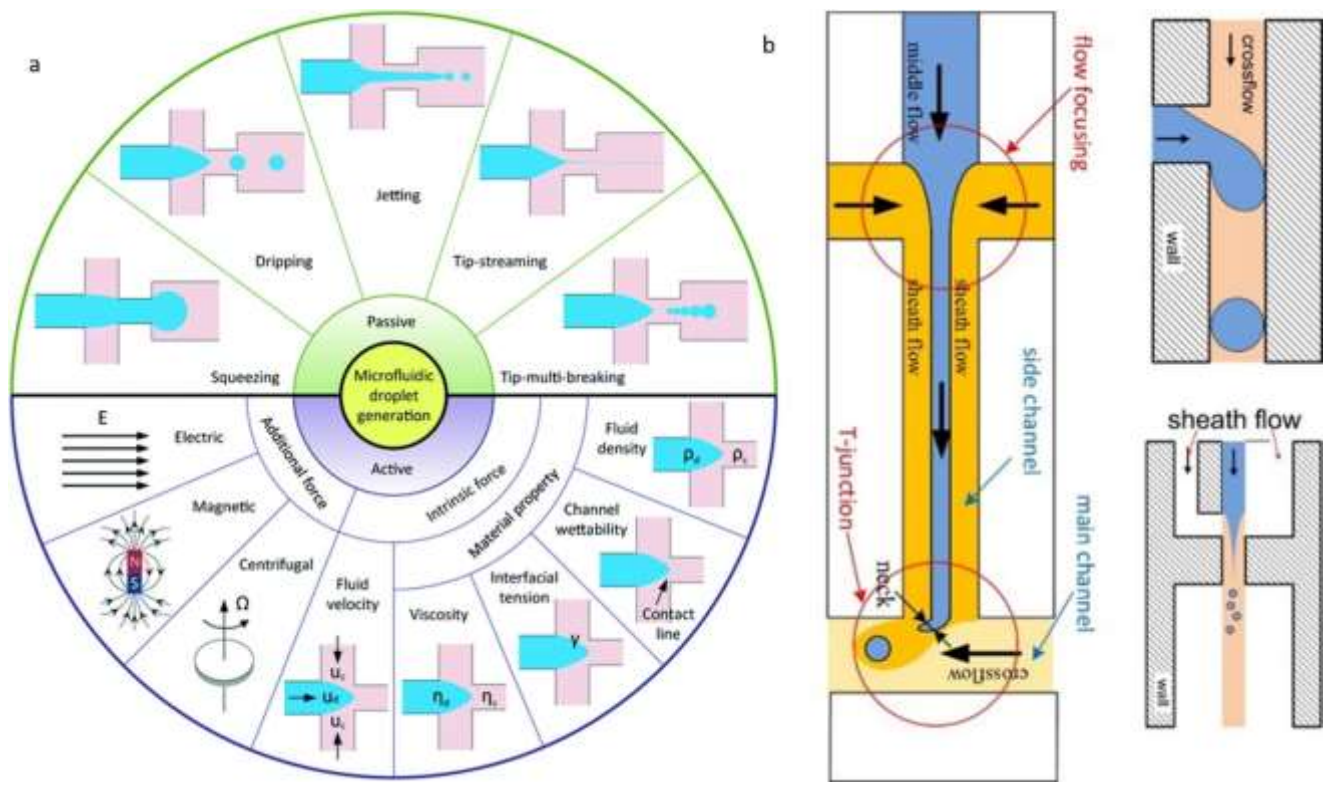


Fig. 3 (a) various type and ways of creating droplets (reproduced with permission from second control technique (reproduced with permission from control technique (reproduced with permission from control technique (reproduced with permission from control technique).

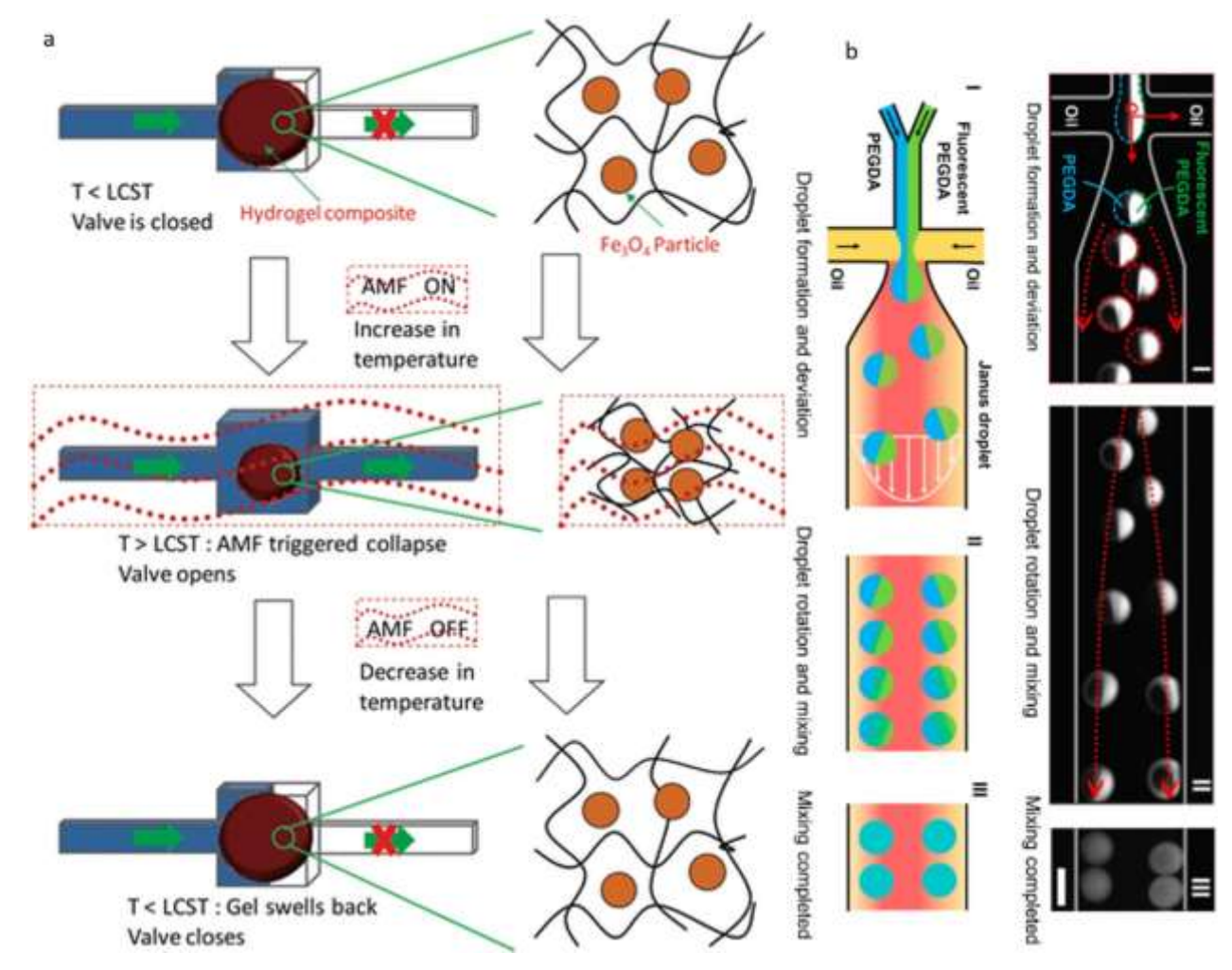


Fig. 4 (a) magnetic driven, an active flow control technique (reproduced with permission from  $^{70}$ : copyright 2009, Royal Society of Chemistry, (b) droplet-based mixing, passive mixing method (reproduced with permission from  $^{74}$ : under the terms of the CC BY 4.0, (https://creativecommons.org/licenses/by/4.0/)).

The light source was a simple LED diode, so the setup did not depend on a laser or any complicated optical setups.<sup>78</sup> Active mixing is also attainable with many other stimuli, such as laser-sourced light, magnetic, acoustic, electric, and thermal fields.<sup>79–81</sup>

The last but essential transport process is the ability to transfer heat, and the capability to transport heat strongly depends on the surface area to volume ratio available for heat transfer. At the microscale, the surface-to-volume ratio is very high (20,000 m<sup>2</sup>/m<sup>3</sup>) over the conventional reactors (1000 m<sup>2</sup>/m<sup>3</sup>).<sup>82</sup> This will facilitate the reactant molecules to experience Isothermal temperatures during the reaction to generate a product of uniform quality, as the reaction rate is very much dependent on the temperature. However, due to the laminar flow conditions in the microfluidic reactors, heat transfer coefficients tend to deteriorate because of the increase in thickness of the thermal boundary layer with time. Active and passive heat transfer enhancement and heating strategies could be used to provide uniform heating and cooling experience for the precursor reagents during the reactions and enhance the heat transport. In addition, the mass transfer can also be improved at higher temperatures by enhancing the mixing of different chemical reagents. The active or non-contact heat transfer enhancement can be achieved through light, induction heating, and dielectric

microwave heating.<sup>83</sup> An example of microwave heating of non-aqueous droplets is shown in **Error! Reference source not found.**b. An Indium alloy electrode integrated with the device locally provides microwave power making it locally heat the samples, enhance the reaction rates and produce a higher yield of nanoparticles.<sup>84</sup> These localized heating approaches make the process more robust and energy-efficient.<sup>85,86</sup> **Error! Reference source not found.**c shows another example of an efficient heat transfer process to maintain isothermal temperatures by artificial solar light source<sup>87</sup>. The microfluidic reactor has a nucleation and growth zone that can absorb light. These localized rapid heating techniques provide the constant temperatures required for each zone.

One widely used passive strategy is modifying the reactor's geometry using flow manipulation or obstruction to achieve non-laminar flow and enhance the heat transfer coefficients. Marschewski et al.<sup>88</sup> investigated the effect of herringbone structures (**Error! Reference source not found.**d) on heat transfer using dry-etched microchannels. The devices with the geometry modification showed a significant increase in the ratio of convective heat transfer to the conductive heat transfer (Nusselt number, Nu). This is clearly indicated by Nu = 32.2 over just Nu of 6.6 for the device with no modification. This enhancement is made

possible by manipulating flow into chaotic helicoidal fluid path patterns.

reaction and assembly of various nanomaterials realized using microfluidics.

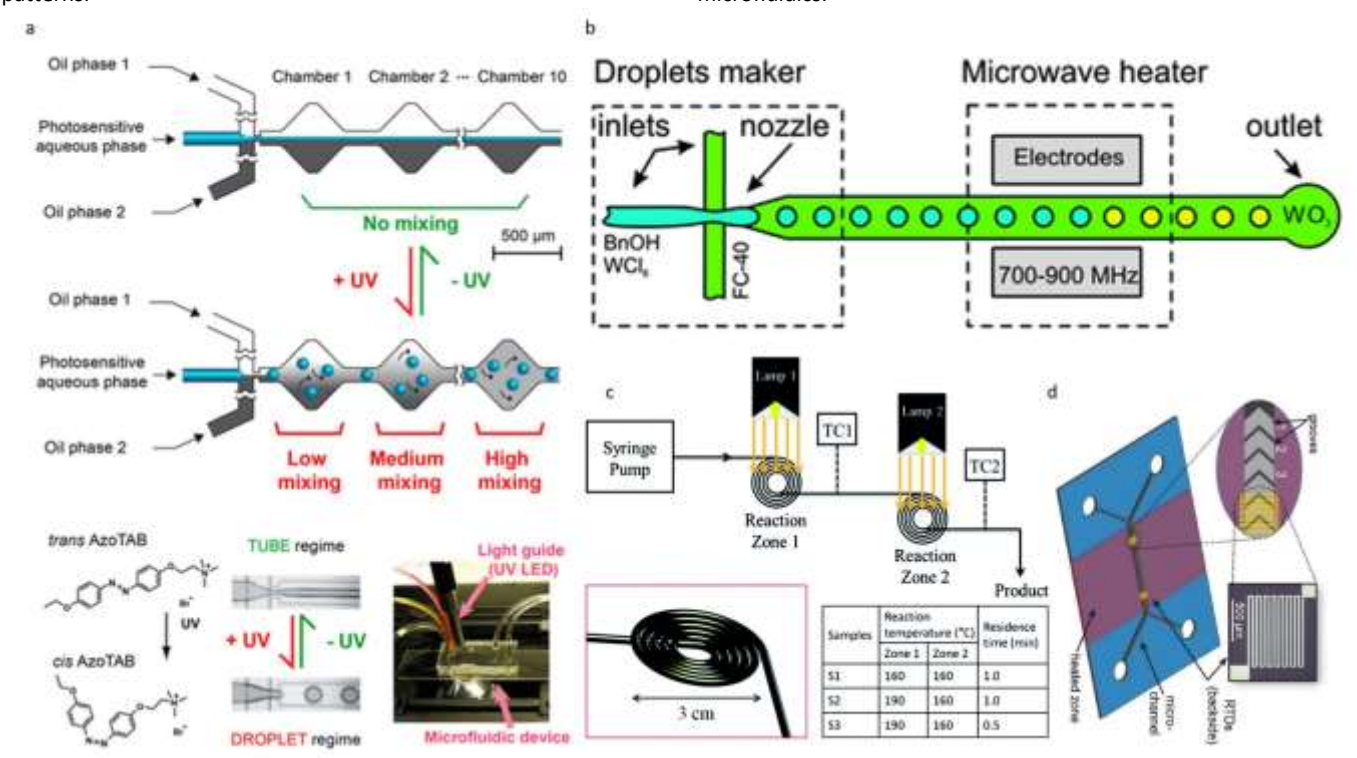


Fig. 5 a) photo mixing, an active mixing method (reproduced with permission from \*\*: copyright 2013, American Chemical Society), (b) microwave dielectric heating, active non-contact heating (reproduced with permission from \*\*: copyright 2013, Royal Society of Chemistry), (c) solar heating (reproduced with permission from \*\*: copyright 2014, , Royal Society of Chemistry), (d) geometry modification, a passive heat transfer enhancement (reproduced with permission from \*\*: copyright 2015, Elsevier Ltd).

While no universal specific control factors govern the reaction and assembly of nanomaterials, each reaction is different. The transport phenomena discussed above, along with reaction kinetics and thermodynamics, play a deciding individual or integrated and interdependent role in dictating the end product's characteristics. Microfluidics makes these types of investigations more efficient and controlled to unravel the mechanisms of these synthesis processes, which will be insightful for scalable nanomanufacturing. These studies will also provide whether micro-scale reactors are necessary to replace a large batch-type reactor to produce nanomaterials for a particular reaction mechanism. The following section discusses the recent progress in exploiting the transport processes to control the

## 4. Recent progress in bottom-up controlled synthesis and assembly

This section discusses the recent progress in the controlled nanomanufacturing of a wide range of nanomaterials such as metals, metal oxides, metal chalcogenides, and nanocomposites. using some selected case studies. Researchers over the past decade made significant contributions to the field by investigating different techniques to regulate the synthesis of nanomaterials.

Table 2 lists the library of nanomaterials synthesized using microfluidic reactors.

Table 2 List of nanomaterials synthesized using microfluidics

| Nanomaterial         | Strategy             | Control Method            | Features                 | References |
|----------------------|----------------------|---------------------------|--------------------------|------------|
| Cu nanocolloids      | T-shaped stainless-  | -                         | 4.25 nm                  | 89         |
|                      | steel reactor        |                           |                          |            |
| Cu NPs               | Lab-on-chip          | Flow rate control         | 9-14nm                   | 90         |
| Ni nanocrystals      | Glass reactor        | Ligands                   | FCC tetrapods            | 91         |
| Pd, Au, Pd-Au, Pd-Pt | PTFE tube            | Segmented flow            | Sphere, cubes, octahedra | 92         |
| Au                   | Lab-on-chip          | Flow rate & channel width | 11.5 nm                  | 93         |
| Au                   | Glass capillary      | Varying reactor geometry  | -                        | 94         |
| Pd                   | Copper capillary     | Controlled concentration  | 5-200 nm                 | 95         |
| Ni                   | Stainless steel tube | Flow rate                 | 6.43-8.76 nm             | 96         |
| Ag                   | Lab-on-chip          | Flow rate                 | 5 nm                     | 97         |
| Ag                   | Lab-on-chip          | Flow rate                 | 2-10 nm                  | 98         |
| Ag                   | Tygon tube           | Flow rate                 | 2-15 nm                  | 99         |

| CrystEngComm             |                                |  |  | Highlight  |
|--------------------------|--------------------------------|--|--|------------|
| Au<br>Au                 | PTFE tube<br>PEEK tube         | Two-stage reactor Co as sacrificial template | < 5 nm<br>Hollow gold NPs  | 100<br>101 |
| Au                       | FEP tube                       | Segmented flow                               | 3-25 nm  | 102<br>103 |
| Pt                       | Silicon-pyrex tube             | Reducing agents                              | -  | 103        |
| Pt<br>Au                 | PTFE tube<br>Lab-on-chip       | Flow rate<br>Flow rate                       | 3.5-5 nm<br>Spherical, 13-40 nm and<br>1.4-4.3 aspect ratio of<br>nanorods | 104        |
| AuPd                     | Lab-on-chip                    | Cyclone mixer                                | 1 nm   | 106        |
| Au, Pd, AuPd             | Lab-on-chip                    | Cyclone mixer                                | 5-7 nm   | 107        |
| Au/Ag                    | Lab-on-chip                    | Combinatorial                                |  | 108        |
| Magnetic iron oxide      | PTFE tube                      | Helical microreactor                         | 141 nm   | 109        |
| ZnO                      | Stainless steel tube           | Deans number                                 | Tactoid and Spherical assembly   | 110        |
| ZnO                      | Lab-on-chip                    | Flow rates                                   | Seven distinct micro/nano<br>ZnO structures were<br>formed                 | 111        |
| Hollow SiO <sub>2</sub>  | Lab-on-chip                    | Spiral microreactor                          | Hierarchical pore sizes less than about 100 nm                             | 112        |
| SiO <sub>2</sub>         | Lab-on-chip                    | Flow rates                                   | nanofibers   | 113        |
| SiO <sub>2</sub>         | Lab-on-chip                    | Surfactants concentration                    | Film, platelets, spheres, and rods   | 114        |
| SiO <sub>2</sub>         | Lab-on-chip                    | Surfactants concentration                    | Biomimetic hierarchical shape  | 115        |
| TiO <sub>2</sub>         | Lab-on-chip                    | Precursor flow rates                         | Nanotubes  | 116        |
| Hollow silica NPs (HSNP) | Stainless steel tube           | Hydrodynamic flow focusing                   | Uniformly dispersed 30nm<br>HSNPs  | 117        |
| ZnO QDs                  | PTFE tube                      | Ultrasonic power and flow rate               | -  | 118        |
| CdSe                     | SS tubing                      | Temperature control                          | Angular, tripod, irregular polygon, and spherical NCs                      | 119        |
| CdSe QDs                 | Lab-on-chip and capillary tube | Fatty acid amine ligands                     | Spherical  | 120        |
| PbS CQDs                 | Capillary tube                 | Dual stage with temperature control          | Spherical  | 121        |
| Ag-ZnO                   | Capillary tube                 | Flow rate                                    | Flower, nanorod array nanostructured films                                 | 122        |
| TiO₂@Au NPs              | PTFE tube                      | pH control                                   | 50-70 nm core with 40-100 nm branches                                      | 123        |
| LaF₃/LaPO₄: Ce, Tb       | PTFE microcapillary            | Contact & non-contact heating                | -  | 124        |
| LaPO <sub>4</sub> : Eu   | Microcapillary                 | Residence time                               | 4 nm dia and 6 nm length   | 125        |
| YVO <sub>4</sub> : Eu    | Stainless steel tube           | Heat flux and flow rates                     | Oval shape NPs   | 126        |

#### 4.1 Metals

Metal Nanoparticles/nanostructures found applications in various fields, such as drug delivery, catalysis, photovoltaics, and electronics. Silver (Ag), gold (Au), platinum (Pt), palladium (Pd), copper (Cu), and Nickel (Ni) NPs are used in many applications because of their properties such as electrical conductivity, anti-microbial and localized surface plasmon resonance (LPSR) and high reflectivity. 127–130 The size, shape, and morphology of these nanomaterials impact the efficiency of an application where they are being used.

Over the years, many chemical solution methods have been developed to synthesize Ag NPs. Tollen's and Modified Tollen's reactions (shown below) produced the NPs without organic ligands. However, these reactions are rapid, and hard to control the residence time precisely to control the nucleation and, thereby, the size of Ag Nps. It is well-known that the nucleation and growth process can effectively regulate nanoparticle size and size distribution. To approach this, in a conventional flask-type reactor, the residence time is controlled by the reaction time, while in a microfluidic reactor, it is governed by the fluid flow (such as flow rates) of the precursors and/or the reactor length. Varying residence time through flow rate tuning is the most common and primary control mechanism.

$$HCHO + 2[Ag(NH_3)^2]^+ + 2OH^- \rightarrow HCOONH_4 + 2Ag + 3NH_3 + H_2O$$

Choi et al.  $^{99}$  investigated the above silver mirror reaction, and the flow rates are used to govern the residence time to control the nucleation and growth (Fig. 6a). This microfluidic synthesis and UV-Vis spectroscopic measurements revealed the residence time

conditions to prevent the aggregation of nanocrystals. Fig. 6b & 6c show that more pronounced peak at 450 nm when a flow rate of 0.4 mL min<sup>-1</sup> while no prominent peak corresponds to a higher flow rate of 0.73 mL min<sup>-1</sup>. Another meaningful learning from this investigation is that microfluidic synthesis can directly deposit nanofilms. In contrast, the batch process requires a foreign-methods such as spin coating and dip coating or other solution deposition techniques. With the capability of controlling aggregation without organic binders, a film with good adhesion quality is developed. Fig. 6d-6f shows the growth of coverage of silver islands on the substrate and respective optical properties of the deposited film. The coverage of Ag islands increased with an increase in deposition periods.

Segmented flow microfluidic reactors are another type of transport control to produce controlled size and shape. In this method, the droplets act as individual microreactors and provide homogeneous temperature and mixing that will enhance product quality in terms of size, shape, and morphology. Zhang et al. <sup>92</sup> investigated the synthesis of gold and palladium NPs in a droplet-based microreactor, as shown in Fig. 7a. As discussed in the previous section, various methods exist to create these types of droplets in microfluidics. This study approached the path of using multi-phase liquid-liquid segment possible by surface tension difference between oil and water-based flow. The pre-mixed reactants mixed in a T-mixer enter another T- mixer where they meet the continuous phase of

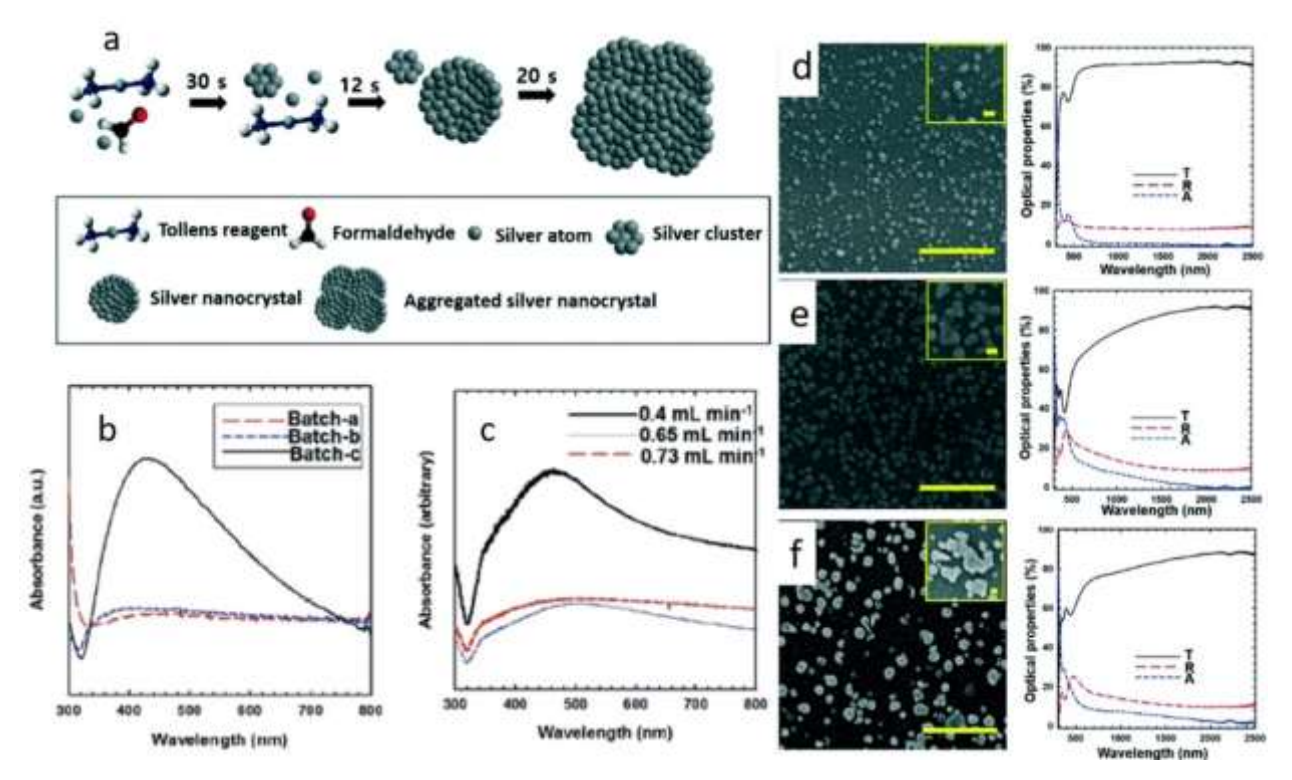


Fig. 6 a) Reaction mechanism of silver nanocrystal formation, b, c) UV-Vis spectra of silver mirror reaction progress, d, e, f) SEM micrographs (1 μm scale bar) and optical properties of silver nanocrystals at different times 2, 5, 9 min (reproduced with permission from: 99 copyright 2017, Royal Society of Chemistry).

silicon oil to create discreet droplets of reactants. The size of particles can be varied by using Au clusters as initial seeds for growth and the exploitation of formed NPs from clusters as seeds for further growth. They observed that the size and shape were also influenced by changing the seed solution concentrations and the reductant concentrations. Fig. 7b shows different sizes and shapes of Au Nps produced using droplet reactors with varied concentrations of reductant and seed solution by altering the kinetics. As reducing agents used in nanomaterial synthesis influence the size and shape of nanostructures, researchers have also studied gas-liquid systems to control and manipulate the morphology of nanostructures by varying the mixing conditions to adjust the mass transfer between the precursor and reducing agents. Sebastian et al.<sup>131</sup> used this gasliquid segmented flow with enhanced mass transfer between the continuous and discreet phases to produce various sizes and shapes of faceted Pt and Pd by varying the gas type. More recently, Huang et al. 102 investigated a gas-liquid segmented flow system (Fig. 7c) to synthesize uncapped Au Nanoparticles rapidly. This investigation has two important observations in terms of flow control and mass transfer control. Firstly, as the ratio of liquid-to-gas flow rates decreases, the mass transfer between the two phases is enhanced because of the larger surface to volume to ratio. Secondly, the reaction conditions, such as pH, can be varied and significantly influence the growth and nucleation process, particle size, and distribution. This outcome is imperative for reactions influenced considerably by pH, such as synthesizing Au NPs using HAuCl<sub>4</sub>. The reactivity of this precursor is very high at lower pH.<sup>102</sup> Fig. 7d shows the integral relationship between the concentration of precursors, liquid-to-gas flow rate, and pH. As the concentration decreases, the minimum particle size moves to the left. This result indicates the integrated relationship between the concentration of Au precursor and the ratios of liquid-to-gas flow rates.

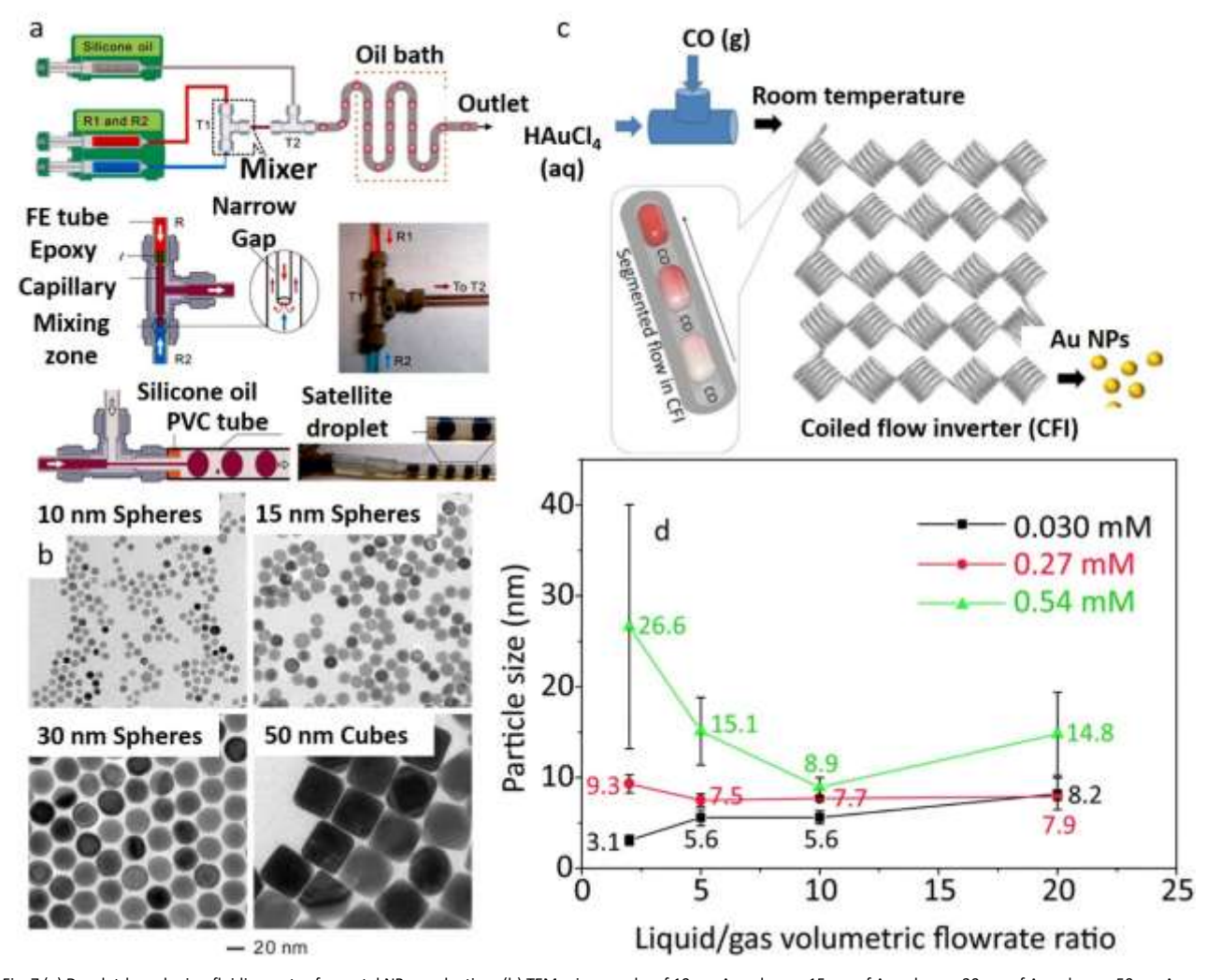


Fig. 7 (a) Droplet-based microfluidic reactor for metal NPs production, (b) TEM micrographs of 10 nm Au spheres, 15 nm of Au spheres, 30 nm of Au spheres, 50 nm Au Cubes (reproduced with permission from: 92 copyright 2014, American Chemical Society). (c) Gas-liquid segmented flow system for Au Nps, (d) size of Au Nps at different liquid to gas flow rate ratios and precursor concentration (reproduced with permission from: 102 under the terms of the CC BY 3.0, https://creativecommons.org/licenses/by/3.0/).

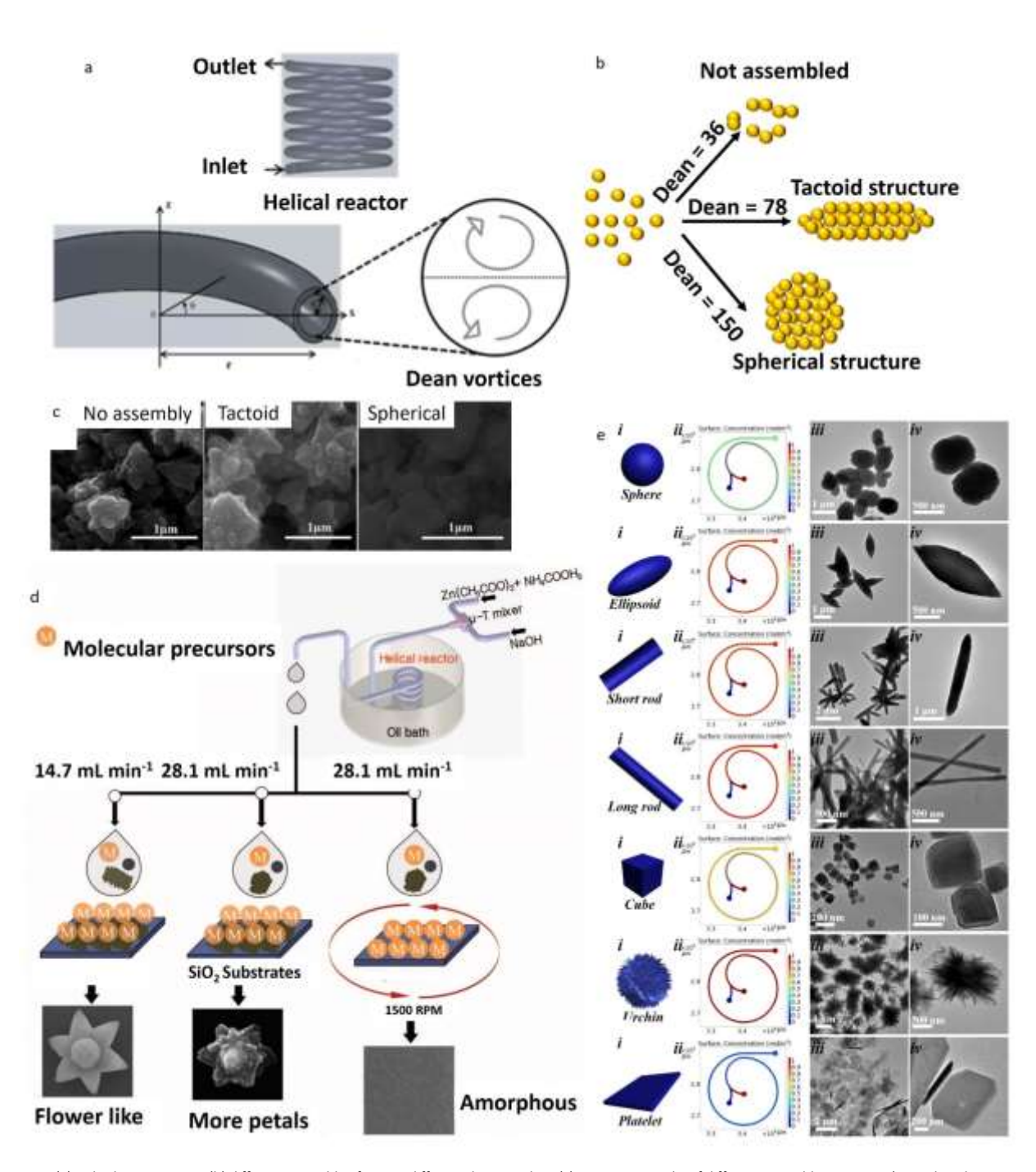


Fig. 8 (a) Helical microreactor, (b) different assembly of ZnO at different dean number, (c) SEM micrographs of different assembly structures (reproduced or adapted with permission from 110: copyright 2013, Royal Society of Chemistry) (d) Different types of nanocrystal assembly and nanostructured thin films (reproduced with permission from 136:copyright 2014, American Chemical Society) (e) TEM micrographs and COMSOL concentration profiles of various reaction conditions (reproduced with permission from 111:copyright 2019, Elsevier).

#### 4.2 Metal oxides

Metal oxide (MO) nanostructures have been used in various critical fields, such as sensors, photovoltaics, electronic and optoelectronic devices, supercapacitors, and energy storage devices. The essential advantage of microfluidics is the capability of tuning nanostructures, and have been significant research in terms of adjusting the shape and assembly of MO nanostructures for diverse applications.

The above section discusses how fluid flows control the metal nanostructures' size and shape. This section outlines how Dean vortices formed inside a curved microreactor due to the secondary flow would influence the MO nanomaterials assembly due to mass transfer enhancement. The segmented flow discussed in the previous section depends on the continuous and discreet phases and the ratio of their flow rates. While the dean vortices rely on the geometry of the reactor and flowrates as the dean number, which is characteristic of dean flow, is a function of the Reynolds number and mean radius of curvature of the reactor. Choi et al. 110 used a helical microreactor (Fig. 8a) to study dean vortices' effect on ZnO nanocrystal assembly. They varied the flow rate to achieve different dean numbers (36, 78, and 150) at a constant pH. This approach resulted in three-dimensional nanostructures, as shown in Figures Fig. 8b & 8c. This assembly is due to enhanced mixing due to dean vortices that lead to collisions of ZnO nanocrystals with each other and the frequency with which those collisions occur. Later, based on this work, the authors assembled different nanostructured films of ZnO from different shapes of ZnO nanocrystals by varying the growth conditions, as depicted in Fig. 8d. The results also showed that deposition on a stationary substrate led to a crystalline film, while an amorphous film formed when the substrate was spinning at the same fluid flow rate condition. In another study, Hao et al.<sup>111</sup> synthesized the ZnO micro/nanostructures in a spiral microfluidic reactor and studied the different morphology of particles for various applications. In contrast to previous works<sup>110,136</sup>, which focused on investigating the Dean number effect on assembly at constant pH, this work investigated formation and assemblies at different ratios of concentrations of reactants which lead to the formation of spherical to platelet shape particles as shown in Fig. 8e. As the flow rate ratios were changing, the formation and assembly of these nanomaterials could have been influenced by the reaction pH that would heavily influence the kinetics of the reaction. The authors also reported a 95-98% yield for these seven different morphologies, which could produce several grams of these materials daily.

#### 4.3 Metal chalcogenides

Metal chalcogenide (MC) nanostructures are essential in nanomaterials as they display unique electronic and optical properties. These unique properties allow them to gain increasing research interests in sensing, optoelectronic devices, electrocatalysis, solar cells, energy storage, and many other applications. <sup>137–139</sup> For all these applications, physicochemical properties, such as particle size, shape, dispersity, and surface chemistry, are again essential factors in determining the efficacy of these materials. Several studies have been conducted to produce MC nanoparticles (CdSe, CuInSe<sub>2</sub>) in microfluidic reactors, such as capillary reactors to solar microflow reactors. <sup>87,140–143</sup>

Uniform temperature plays a vital role in controlled nanomaterials synthesis. Here, two case studies of controlled temperature synthesis of MCs are selected to discuss the temperature effects. Fig. 9a illustrates the schematics of a microfluidic reactor setup for producing CdSe nanocrystals. In this study, Wang et al. 119 pre-prepared CdSe precursor solution by mixing Cd precursor solution with Se precursor solution. The precursor solution then flows through the microreactor maintained at a sufficient temperature to promote nanocrystal formation and growth. Nanocrystals with different morphologies (Fig. 9b) were produced at different temperatures, showing photoluminescence spectra changing from bright green to red. These results indicate that precise heat transport is essential in producing similar shapes and sizes of nanostructures.

Furthermore, a critical advantage of microfluidic reactors is numerous pathways to separate the nucleation and growth stages to get better control over nanomaterial synthesis and ease of scalability. One of the ways to achieve this is by multi-stage localized temperature control. Pan et al.<sup>121</sup> demonstrated a two-stage microfluidic reactor (Fig. 9c) to control the dispersity of PbS colloidal quantum dots (CQDs) compared to a batch reactor. Fig. 9d-f shows that produced CQDS is comparable to batch synthesis and shows monodisperse nanostructures after purification and redispersion. The authors claim the yield is about 2.5 times higher than batch reactors. This example shows the promise of microfluidics from converting lab-scale synthesis to commercial scale.

#### 4.4 Composite and doped nanomaterials

The following covered material class consists of nanomaterials that combine different materials, taking advantage of their complementary properties and behaviors. They can consist of materials from separate classes (e.g., metals and metal oxides); we will refer to them as composite or doped nanomaterials. Composite nanomaterials contain two constituents at the molecular or nanometer level, combined via different methods. We will cover two classes of composite materials: nanocomposites and core-shell particles. Nanocomposites combine inorganic materials through the incorporation of nanoparticles into a matrix. The addition of nanoparticles can drastically improve material properties such as mechanical strength, thermal and chemical stability, and optical, electrical, or catalytic properties. As such, nanocomposites have seen use in many applications across biomedical, photovoltaic, catalytic, and electronic fields. 144 The size, shape, and morphology of the matrix and nanoparticle phases profoundly influence the resulting nanocomposite performance. Core-shell particles differ from nanocomposites in that instead of incorporating one material into another matrix, one constituent forms an outer shell around an inner core constituent. The core and shell materials can have synergistic or complementary properties. Doped nanomaterials are attained when a different element is introduced into the lattice structure of a host material as an impurity and are typically used to tune electrical properties. Whereas composite nanomaterials have two distinct phases of materials, doped nanomaterials are single phases. Several research groups have demonstrated that the material properties of these composite materials can be controlled by tuning microfluidic

parameters and conditions such as flow rate, heating, and flow behavior.

Fig. 10a illustrates the design of a microfluidic deposition process for the deposition of Ag-ZnO nanocomposite films. <sup>122</sup> Each material stream before entering the micromixer, can be independently varied to have different flow rates, temperatures, tube lengths, and flow behavior, allowing for a multitude of controllable parameters which can play a role in the resultant Ag-ZnO film. For example, by varying the flow rate of the ZnO nanoparticle stream, various ZnO morphologies such as flower-like films, nanorod array films, and amorphous films could be produced (Fig. 10b). The

nanocomposite films retained their structure after the deposition of Ag nanoparticles onto the ZnO matrix and were found to have enhanced photocatalytic activity and efficiency over pristine ZnO films. Marelli et al.  $^{123}$  synthesized TiO  $_2$ -Au nanocomposites using ascorbic acid as a reducing and stabilizing agent (Fig. 10c). Multibranched Au NPs coated by TiO  $_2$  (Fig. 10b &10c) are synthesized by controlling the pH of the reaction by varying the ascorbic acid available for the reaction. Fig. 10 d shows the photocatalytic degradation of rhodamine B at different times, and a comparison of photocatalytic activity reveals that commercial TiO  $_2$  could not degrade as synthesized TiO  $_2$ -Au composites.

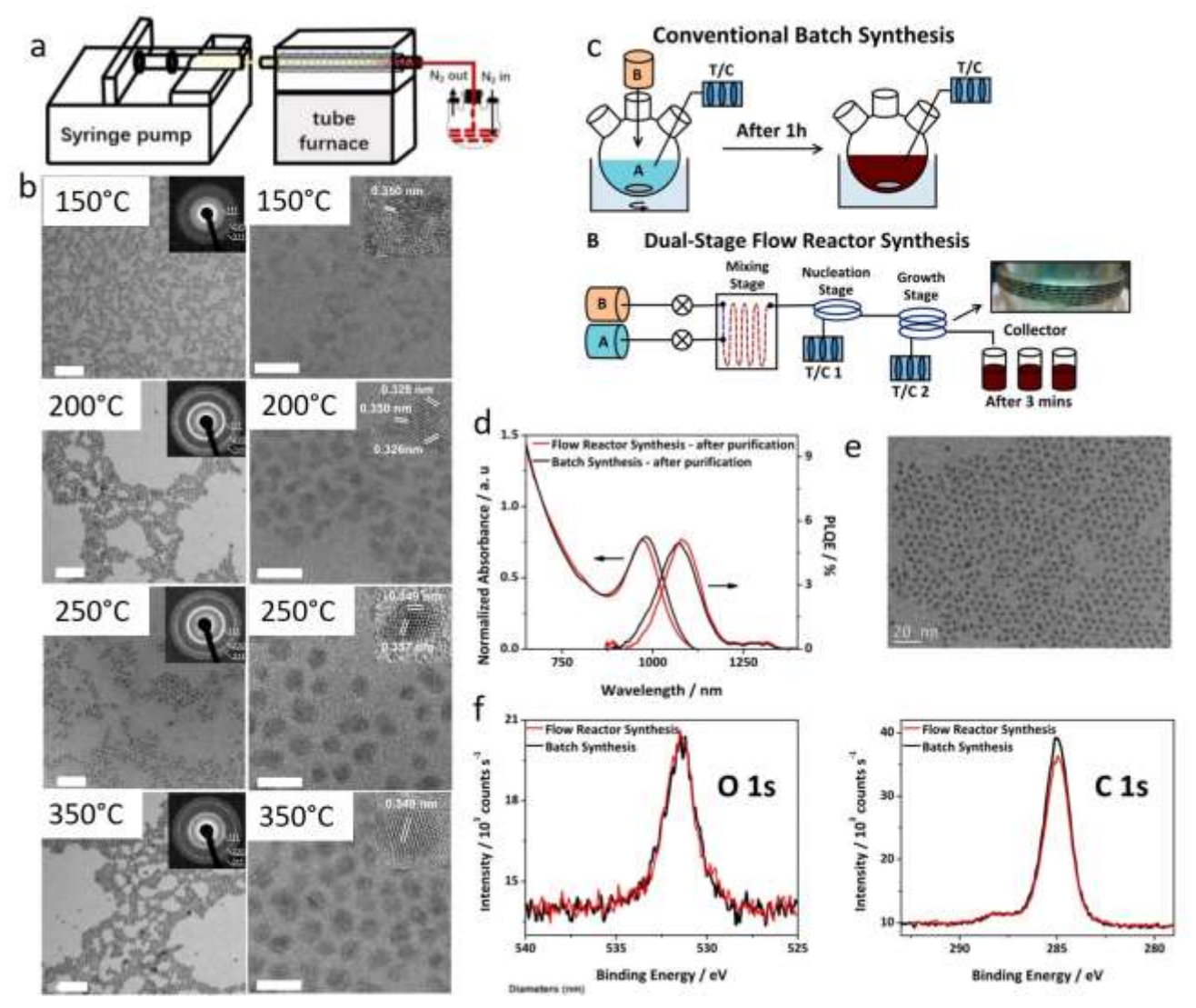


Fig. 9 (a) schematic of microfluidic setup. (b) TEM micrographs of various shapes of CdSe nanocrystals (reproduced with permission from 119 :copyright 2017, American Chemical Society). (c) schematic of microfluidic device for PbS CQDs. (d) PLQE and absorption spectra comparison between batch and microfluidic synthesis, e) TEM micrograph of CQDs produced by microfluidic reactor; scale bar 20 nm, f) XPS spectra (reproduced with permission from 121 :copyright 2013, American Chemical Society).

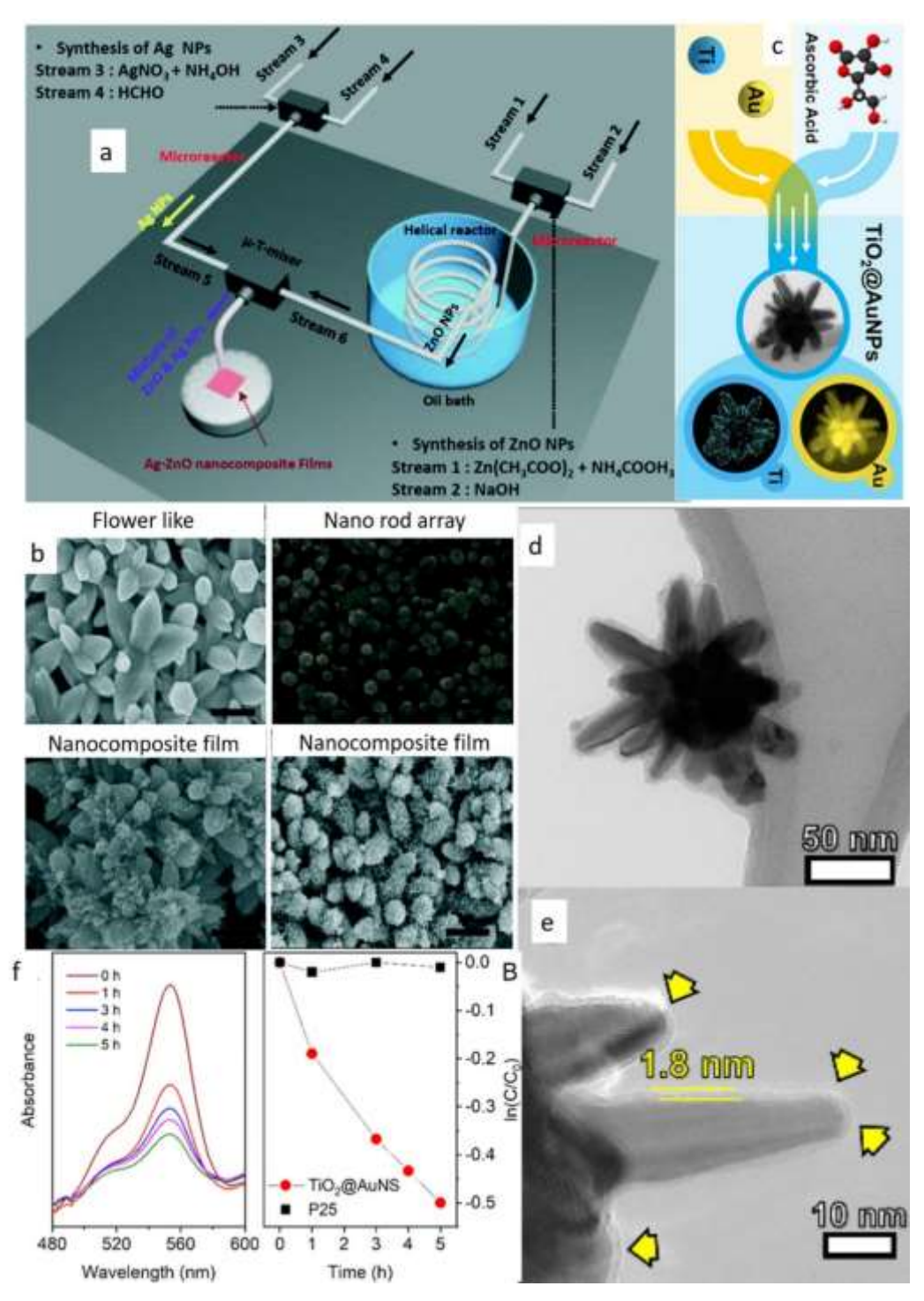


Fig. 10 (a) schematic of Ag-ZnO microfluidic deposition setup. (b) SEM micrographs of ZnO flower-like and nanorod array and Ag-ZnO flower-like and nanorod array films (reproduced with permission from 122:copyright 2019, Royal Society of Chemistry), (c) schematics showing TiO2 @AU NPs, (d) TEM micrograph of nanocomposite, e) HRTEM image of composited with arrows indicating TiO2 conformal layers (reproduced with permission from 123:copyright 2020, American Chemical Society).

The temperature of the reaction can be controlled by varying the heat flux or using more efficient and faster non-contact heating techniques. In this section, we select two case studies of controlled synthesis of nanomaterials to illustrate the temperature and type of

heating effects. He et al.  $^{126}$  used a hydrothermal microreactor, as shown in Fig. 11a, to synthesize yttrium orthovanadate (YVO<sub>4</sub>) nanoparticles doped with europium (Eu). Effects of flow rates and heat flux on morphology, crystallinity, and site symmetry were

investigated thoroughly. SEM micrographs in Fig. 11b show that the aspect ratio of particles increased with higher heat flux, and particles with oval-shaped features are obtained at 1800 W/m<sup>2</sup>. Fig. 11c shows the energy transfer and CIE chromaticity of nanocomposite Fig. 11d illustrates the experimental setup for particles. synthesizing LaF<sub>3</sub>:Ce,Tb and LaPO<sub>4</sub>:Ce,Tb nanocrystals. Reagent solutions are pumped via syringes into a micromixer and then flow through a heat treatment step before being deposited in a sample bottle. 124 The heat treatment is either microwave irradiation (MW) or oil bath (OB) heating, and the type of heating impacted the

resulting morphology and crystallization of the nanocomposites. Overall, microwave irradiation resulted in more monodisperse and higher crystallinity LaF<sub>3</sub>:Ce,Tb nanoparticles. In LaPO<sub>4</sub>:Ce,Tb nanorod systems, microwave irradiation resulted in more monodisperse and smaller nanorods with higher crystallinity. Using oil bath heating resulted in larger nanoparticles of varying morphologies, which included nanorods, nanowires, and nanosheets (Fig. 11e). This study shows the type of heating could impact material properties such as size, shape, dispersibility, and crystallinity.

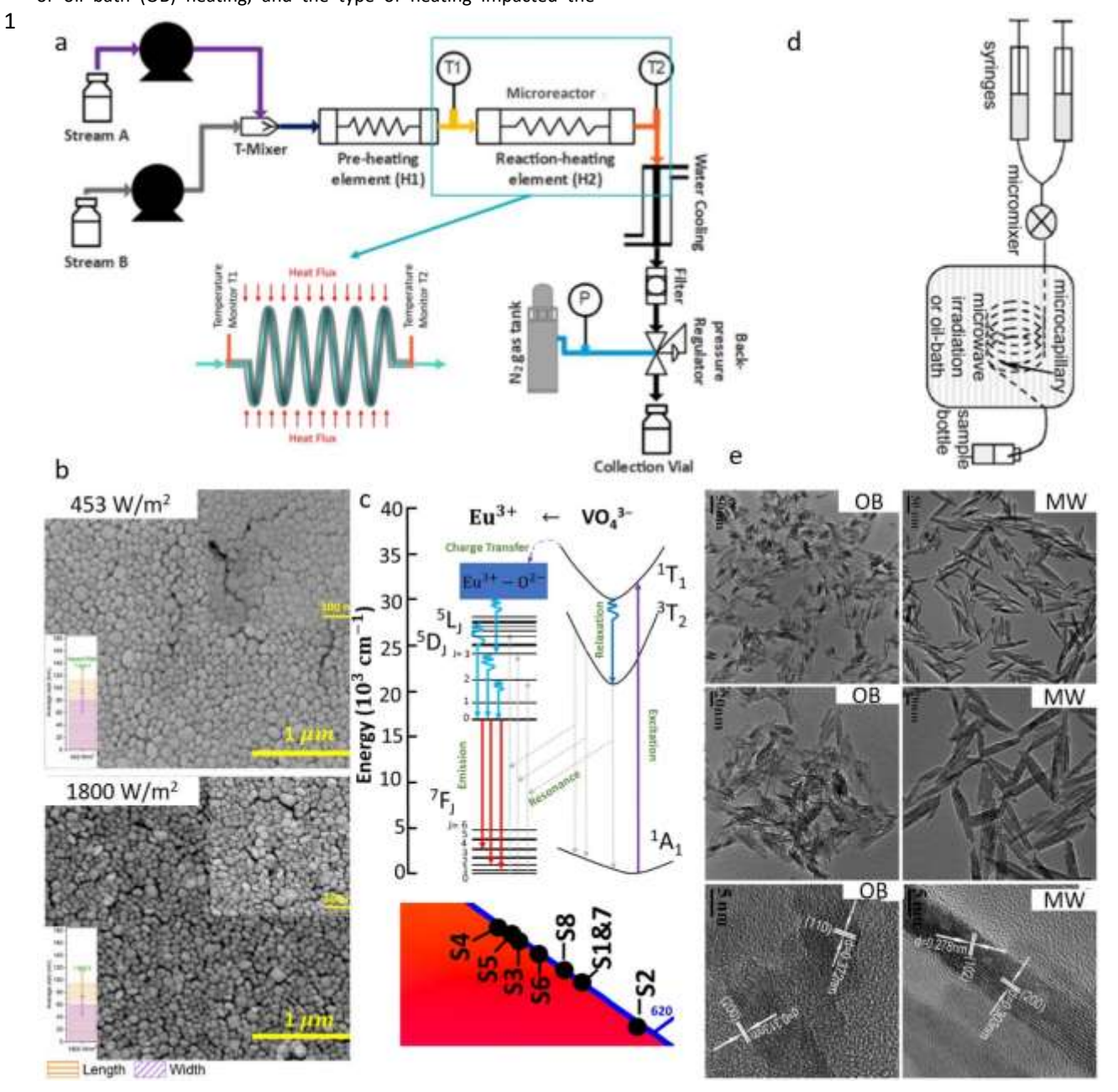


Fig. 11 (a) Schematics of hydrothermal microreactor, (b) SEM micrographs of NPs synthesized at different heat flux conditions, (c) energy transfer in NPs at NUV/UV and CIE chromaticity diagram ( reproduced permission from 126:copyright 2020, IOP Publishing). (d) schematic of microfluidic device for LaF3:Ce,Tb and LaPO4:Ce,Tb syntheses. (e) TEM and HRTEM micrographs of LaPO4:Ce,Tb nanorods prepared by both microwave irradiation (top images) and oil bath heating (bottom images) (reproduced with permission from 124: copyright 2009, Royal Society of Chemistry).

# 5. Recent progress in top-down microfluidic exfoliation of two-dimensional nanosheets

The remarkable physical and chemical properties of two-dimensional (2D) materials enable advanced electronic, catalytic, energy, and biomedical applications. 145–147 To harness these properties, mono- or few-layer 2D nanosheets must be delaminated from bulk materials. Among various exfoliation technologies, liquid phase exfoliation (LPE) is the most widely used to produce these 2D nanosheets, but its drawback is apparent with low exfoliation efficiency and low scalability. 15,148

Microfluidics has improved the exfoliation efficiency of 2D materials because it can induce a more uniform driving force for exfoliation in a small active area.61 In addition, by precisely controlling and manipulating microfluidic flow, it is possible to produce high-quality two-dimensional nanosheets with low defects and large lateral sizes within an integrated system. 64,65,149,150 Some recent representative works exfoliating 2D nanosheets using microfluidic are listed in Table 3. Microfluidic-based exfoliation technology generally utilizes sonication or high-shear mixing energy to fragment and delaminate bulk 2D material into thin-layered one. Cavitation effect or strong shear stress induced by sonication or shear rotor, respectively, can uniformly propagate throughout 2D material dispersion compared to conventional batch exfoliation processes, significantly improving exfoliation efficiency and uniformity of resulting 2D nanosheets. According to Table 3, different microfluidics methods have been employed to produce various 2D nanosheets. Selected case studies of producing 2D nanosheets by various methods are discussed below.

Using the AM process, Choi et al.<sup>64</sup> produced few-layer BP nanosheets and BP quantum dots. The flow rate of the precursor dispersion was found to play an essential role in determining the cavitation effects, and at an optimal flow rate, few-layer BP nanosheets were obtained with a 45% exfoliation efficiency within a 6 min residence time. The efficiency of the AM system was higher at all initial bulk BP concentration ranges than the batch system (Fig. 12a). The flakes obtained by the AM method showed a stripe shape with a lateral size of 492 ± 235 nm. Along with the higher efficiency, the AM process produces 2.5 ± 1.2 nm thick flakes on average, corresponding to 2–4 layers of phosphorene, which is thinner than 7.2 nm thick flakes obtained by the batch exfoliation (Fig. 12b). Fewlayer BP nanosheets were further treated in the AM process to fragment them into smaller ones, eventually forming BP quantum dots. Inspired by these studies, Choi et al. 53,151 manufactured a superhydrophobic silicon nanowire (SiNW) microfluidic device. The superhydrophobic SiNW microfluidic system was devised to supply a bulk material dispersion into a patterned superhydrophobic SiNW microchannel (Fig. 12c). This device is featured with the wise utilization of distinct surface energy differences along the interface of superhydrophobic SiNWs and hydrophilic liquid phase. Thus, as hydrophilic 2D nanomaterial dispersion flows inside the microchannel, it does not wet the superhydrophobic SiNWs and forms a stable air-water interface along the microchannel. The interface between the dispersion and superhydrophobic SiNWs can serve as activation sites for the onset of cavitation bubbles, leading to considerably improved exfoliation efficiency compared to a process without the two-phase interface. Notably, nearly 80% of bulk BP was transformed into thin-layered BP nanosheets within 5 nm thickness in a few minutes of process time.

Graphene is the most widely produced 2D nanosheet by microfluidization. Karagiannidis et al.  $^{62}$  conducted a comprehensive study covering graphene production via microfluidization, graphene ink formulation, and application. Notably, highly concentrated aqueous graphene dispersion was prepared by microfluidization after optimizing the graphite and surfactant ratio and critical processing parameters. After 100 cycles, graphite reduced its lateral size and thickness to approximately 1  $\mu m$  and 12 nm, respectively, with 100% yield (Fig. 13a).

However, the high number of processing repetitions caused the degradation of exfoliated graphene. Thus, mild exfoliation conditions such as reduced cycling repetition were adopted for practical applications to produce conductive graphene ink with high performance.

Del Rio Castillo et al.65 exfoliated various 2D materials, including h-BN, graphene MoS<sub>2</sub>, and WS<sub>2</sub>, via the WJM process. Although detailed information on the yield was not discussed, WJM could produce monolayer or few-layer 2D nanosheets with a concentration of 10 g L-1 and the productivity of 2L h-1, demonstrating the WJM's capability for very fast and scalable production of 2D nanosheets. Thin layers of MoS<sub>2</sub>, WS<sub>2</sub>, and h-BN nanosheets were generated, with lateral sizes reduced to 380, 500, and 340 nm and thicknesses to 6.0, 4.5, and 2.4 nm for MoS<sub>2</sub>, WS<sub>2</sub>, and h-BN nanosheets. Ahmed et al. 152 exfoliated MoS<sub>2</sub> using a chip-scale piezoelectric device as a microfluidic nebulizer at high-frequency (10 MHz) acoustic excitation (Fig. 13b). An acoustic wave generated in the device created high shear stress for the exfoliation of bulk MoS2 and simultaneously led to the formation of MoS<sub>2</sub> microdroplets that were subsequently transferred to a pre-patterned plate for large patterning of MoS<sub>2</sub> nanosheet film. However, this process is limited to 2D materials exhibiting the piezoelectric response of non-centrosymmetric materials such as MoS<sub>2</sub>, WS<sub>2</sub>, and other transition metal dichalcogenides (TMDC). The overall yield was reported to be ~2%, of which ~41% consisted of monolayers.

Although the microfluidic-based approaches can be an alternative to the conventional bath systems for efficiently producing 2D nanosheets, their ability to scalable production of 2D nanosheets has fallen behind demands for practical applications of 2D nanosheets, particularly toward the commercial level. Numbering up of microfluidic devices may be a solution to meet the production demand, but the high equipment cost and energy consumption of WJM or microfluidization is a preliminary issue to be addressed for the numbering up strategy. The AM process uses a laboratory sonic bath that is simple and cheap. Therefore, this AM process may be a cost- and energy-effective means for numbering up. However, the exfoliation efficiency of the AM process is still very low, making the production cost of the 2D nanosheets uneconomical for commercialization. To realize the commercial level of 2D nanosheet production, an advanced microfluidic device should be developed to significantly enhance the production yield with almost 100 % conversion from bulk to 2D nanosheets free of defects.

Table 3 Recently published works on different types of 2D materials produced by microfluidics

| Matavial   | Country attick NA attack | Fea          | Features  |           |
|--|--------------------------|--------------|-----------|-----------|
| Material   | Synthetic Method         | Lateral      | Thickness | Reference |
| Black phosphorene                                  | Acoustic-microfluidic    | - 400 nm     | - 5 nm    | 53        |
| Black phosphorene & Quantum dots                   | Acoustic-microfluidic    | 500 nm       | - 4 nm    | 64        |
| Graphene Quantum dots                              | Microfluidization        | - 3 nm       | - 5 nm    | 153       |
| Graphene   | Microfluidization        | - 7 μm       | - 10 nm   | 63        |
| Graphene   | Lab-on chip              | - 400 nm     | - 7 nm    | 66        |
| Graphene   | Microfluidization        | 0.5 - 200 μm | - 20 nm   | 62        |
| Graphene   | Microfluidization        | 1.24 μm      | - 10 nm   | 154       |
| Graphene   | Microfluidization        |              | - 4 nm    | 150       |
| Graphene, h-BN, MoS <sub>2</sub> , WS <sub>2</sub> | Wet-jet milling          | - 460 nm     | - 5 nm    | 65        |
| h-BN   | Microfluidization        |              | 8-12 nm   | 155,156   |
| MoS <sub>2</sub>                                   | Lab-on chip              | - 200 nm     | - 8 nm    | 152       |

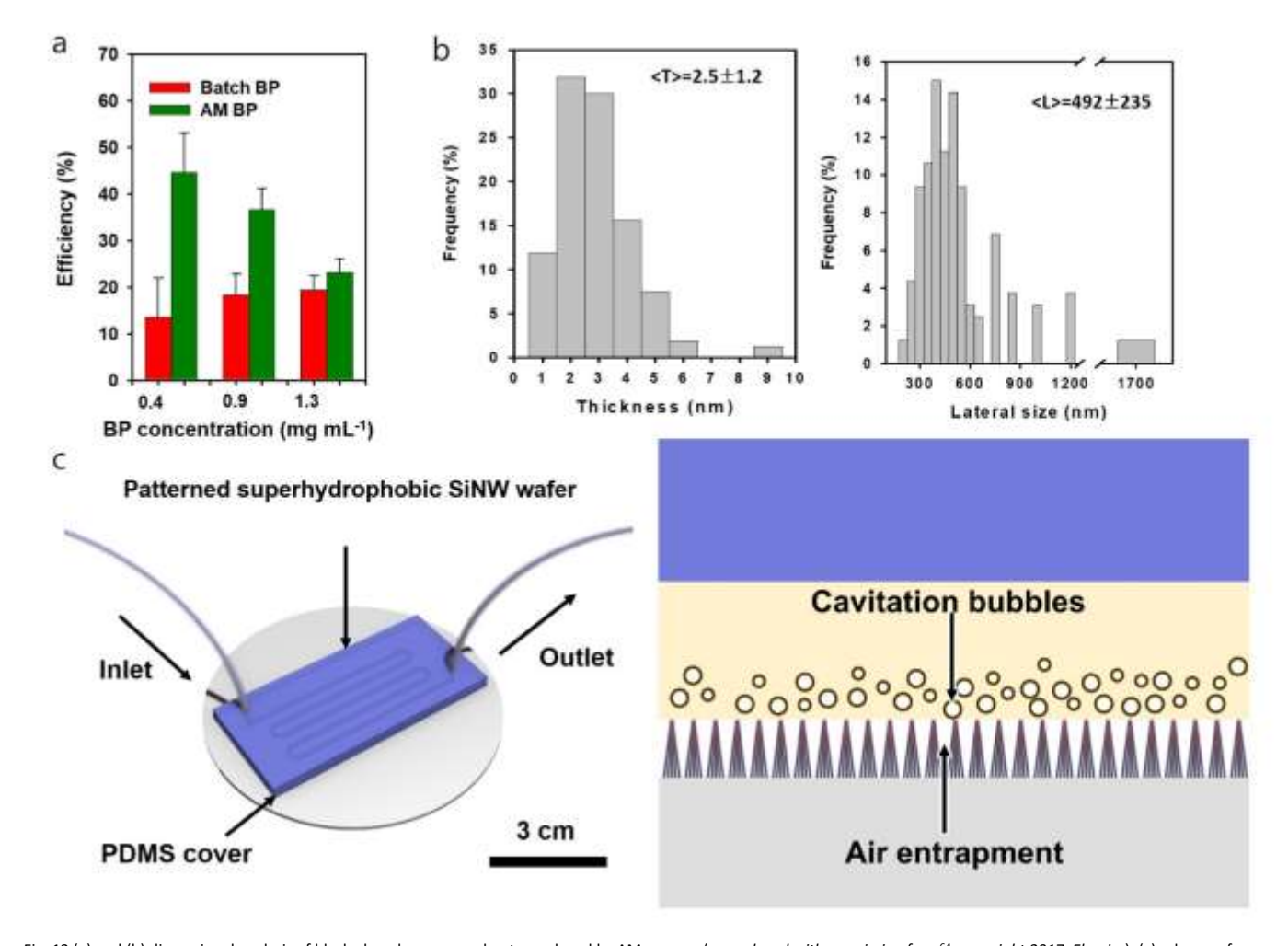


Fig. 12 (a) and (b) dimensional analysis of black phosphorus nanosheets produced by AM process (reproduced with permission from<sup>64</sup>: copyright 2017, Elsevier), (c) scheme of superhydrophobic SiNWs microchannel device to promote cavitation effect over the two-phase interface (reproduced with permission from<sup>151</sup>: copyright 2018, Elsevier B.V.).

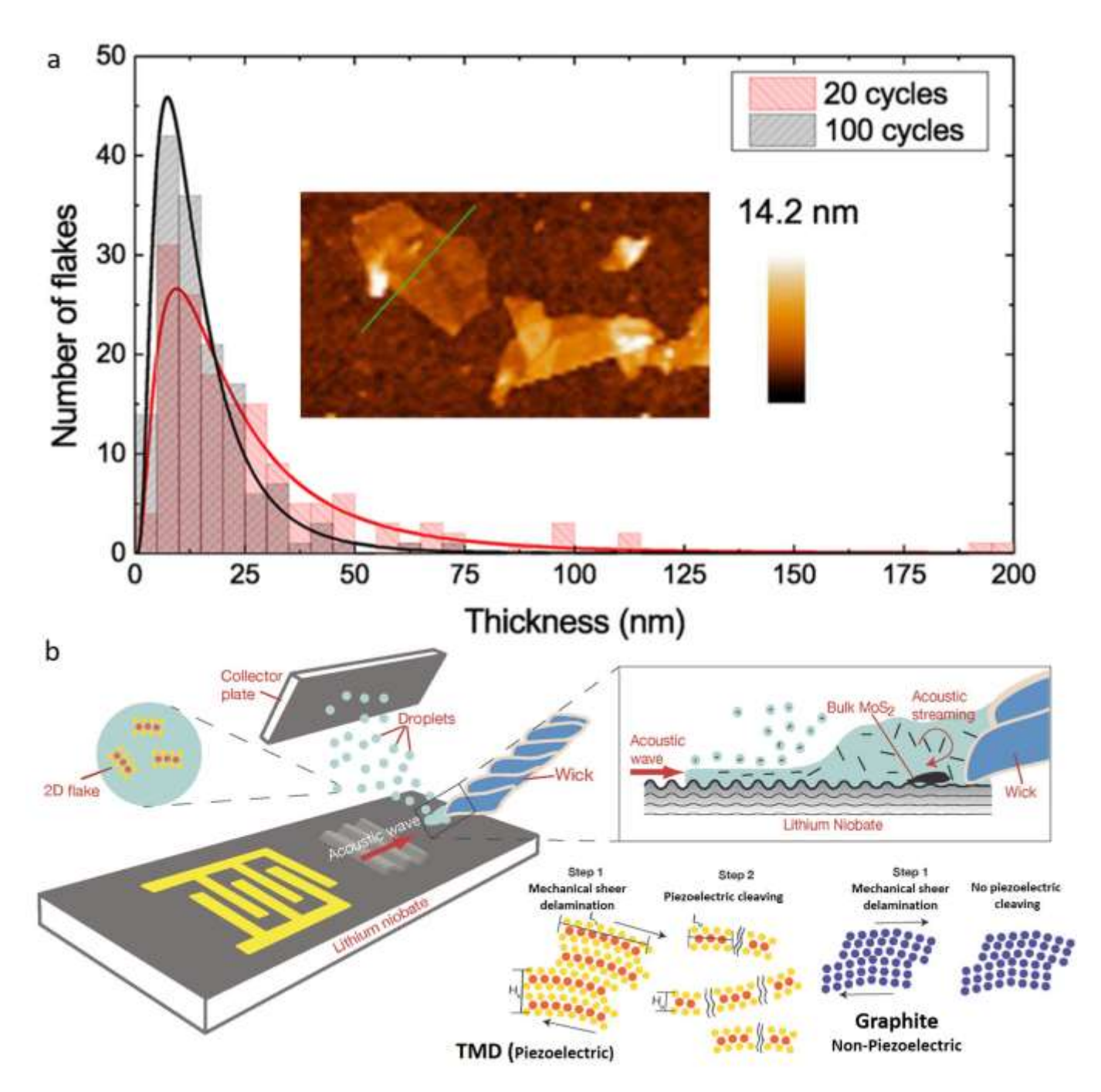


Fig. 13 (a) dimensional analysis of graphene produced by microfluidization (reproduced with permission from 62: copyright 2017, American Chemical Society, CC-BY 4.0, https://pubs.acs.org/page/policy/authorchoice\_ccby\_termsofuse.html), and (b) scheme of chip-scale piezoelectric device for delamination of 2D materials and in-situ patterning of 2D nanosheet film (reproduced with permission from 152: copyright 2018, WILEY-VCH Verlag GmbH & Co. KGaA, Weinheim).

### 6. Outlook and conclusions

Despite the tremendous progress over the last decade, knowledge gaps and challenges still exist and must be solved. More studies of transport studies are required to understand the mechanism of control and assembly for a wide range of materials. For example, mixed metal oxide/chalcogenide nanostructure (quaternary, ternary, or spinel oxides) have many applications, from optoelectronics and catalysis to energy storage. A combinatorial synthesis approach can lead to a better understanding of the connection among syntheses, structures, and material properties of different nanostructure

assemblies and compositions. There are not many combinatorial nanomaterial synthesis studies using microfluidics in the literature. One study that stood out is the 33 Au/Ag ratio multi-colour nanoparticle manufacturing using 2 inlet streams to generate 33 different solutions. This study shows the promising capability of exploiting microfluidics to synthesize and evaluate the performance of these complex oxides and chalcogenides for their application areas.

There is no study on controlling the transport processes of 2D nanosheet exfoliation. 2D nanosheets are exfoliated from their bulk form, top-down, not based on synthesis. In addition, the cavitation effect, an energy source for the exfoliation of 2D nanosheets, is a highly complex phenomenon, and only empirical studies on controlling cavitation have been conducted. Flow rate is a critical factor in governing the magnitude of cavitation, as cavitation bubble dynamics are significantly affected by flow rate. An optimal flow rate range exists, preventing the coalescence of cavitation bubbles and facilitating the cavitation effect. A flow rate spectrum out of the optimal range would sweep the cavitation bubbles before their activation or induce their merging to form large inactive bubbles for the cavitation effect.

It is encouraging to see Fully automated syntheses for regulating the growth and assembly of nanomaterials. However, the studies often do not run long enough to understand the fouling of microchannels, their cleaning or replacement frequency, and their effect on the ability to tune nanomaterials. More research is needed concerning the path forward for the scaling approach of in terms of one-time or reusable reactors. If one-time use, the economics of this method and strategies to recycle those reactor materials remains to be further studied.

Another area that requires more research for the field to grow is in-situ real-time monitoring of controlled synthesis and integrating the data with machine learning models to predict and improve the synthesis conditions with a smaller number of iterations. In-situ monitoring of batch and continuous nanoscale structures using small-angle X-ray scattering (SAXS), wide-angle X-ray scattering (WAXS), X-ray absorption spectroscopy (XAS), transmission X-ray microscopy (TXM), and operando XAS and SAXS are excellent examples.<sup>157–160</sup>

With advances in additive manufacturing and 3D printed microchannels, many innovative designs could be designed and used to control the transport processes and tune the nanomaterials.

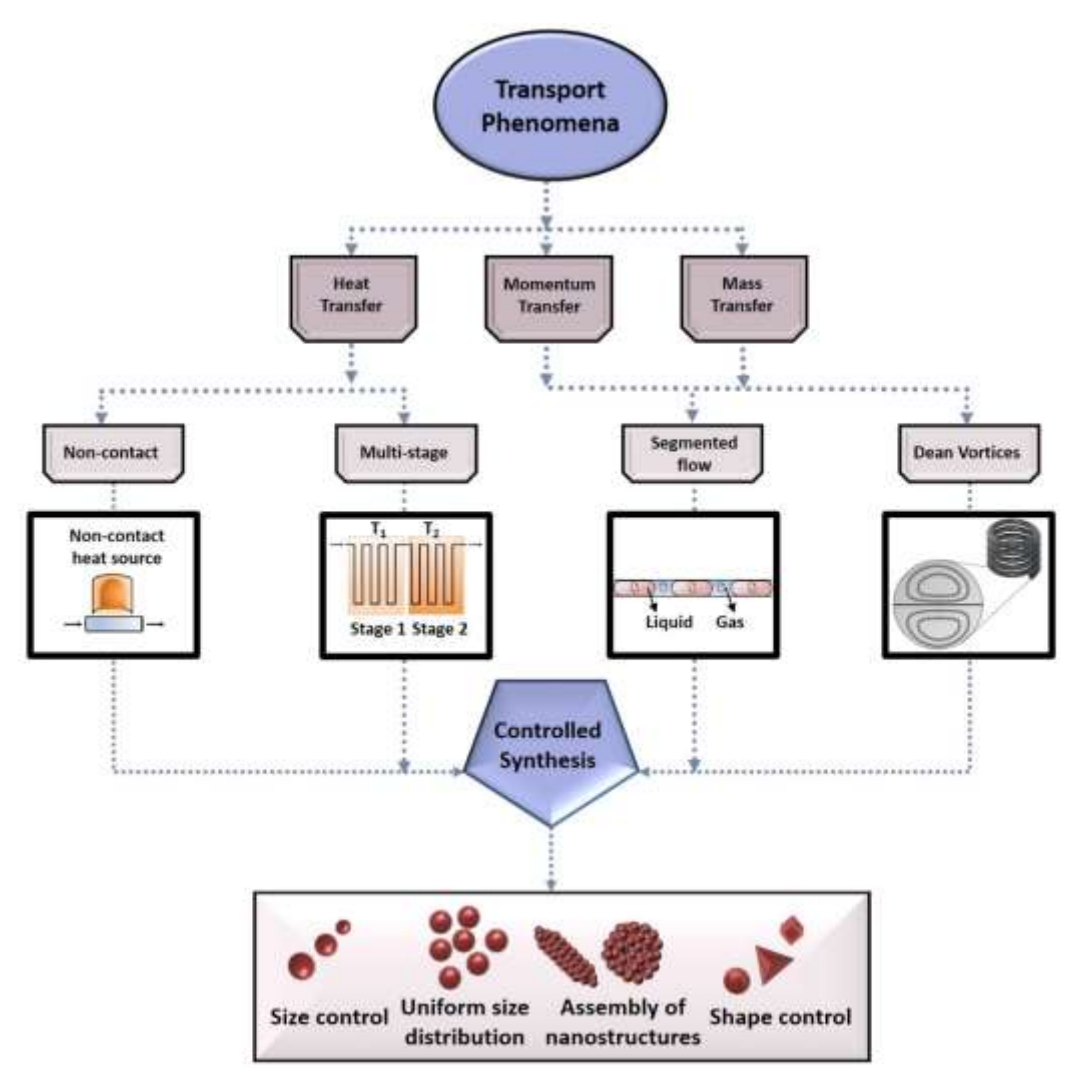


Fig. 14 Tuning transport processes for controlled synthesis.

In conclusion, microfluidics has significantly advanced the synthesis of nanomaterials due to their unique capability to govern transport phenomena. This review discussed the various types of existing methods of transport control and the exploitation of those methods for controlled synthesis of a diverse range of functional nanomaterials. Compared to batch reactors, microfluidics provides exceptional reaction control for precise tuning of the size, dispersity, morphology, and, therefore, functions of materials. Multi-stage

reactors for nucleation and growth separation, non-contact techniques for uniform localized heating, segmented flow reactors, and dean vortices to enhance mass transfer are methods to govern the synthesis. As shown in Fig. 14, the nanomaterials produced by tuning transport processes are promising to generate diverse nanomaterials with size, shape, and nanostructures.

#### **Conflicts of interest**

There are no conflicts to declare.

#### **Acknowledgments**

This research was funded by the National Science Foundation IIP, PFI-RP 1941262, CBET-2151049, and ITE-2236036. Alvin Chang acknowledges support from the NSF Graduate Research Fellowship Program (GRFP) under Award No. 2234662. Chang-Ho Choi also acknowledges support from the National Research Foundation of Korea (NRF) grant funded by the Korea government (No. NRF-2022R1F1A1068280). The authors also like to thank Hsin-Mei Kao for the helpful discussions.

### References

- Z. Y. Zhou, N. Tian, J. T. Li, I. Broadwell and S. G. Sun, *Chem. Soc. Rev.*, 2011, 40, 4167–4185.
- J. Huang, L. Lin, D. Sun, H. Chen, D. Yang and Q. Li, *Chem. Soc. Rev.*, 2015, 44, 6330–6374.
- P. K. Jain, X. Huang, I. H. El-Sayed and M. A. El-Sayed, *Acc. Chem. Res.*, 2008, 41, 1578–1586.
- 4 N. Abid, A. M. Khan, S. Shujait, K. Chaudhary, M. Ikram, M. Imran, J. Haider, M. Khan, Q. Khan and M. Maqbool, *Adv. Colloid Interface Sci.*, 2022, **300**, 102597.
- 5 R. M. Fratila, S. Rivera-Fernández and J. M. De La Fuente, *Nanoscale*, 2015, **7**, 8233–8260.
- 6 Z. Liu, W. Cai, L. He, N. Nakayama, K. Chen, X. Sun, X. Chen and H. Dai, *Nat. Nanotechnol.*, 2007, **2**, 47–52.
- W. W. Zhao, C. Y. Tian, J. J. Xu and H. Y. Chen, *Chem. Commun.*, 2012, **48**, 895–897.
- 8 M. hosein Mohammadi, M. Eskandari and D. Fathi, *J. Alloys Compd.*, 2021, **877**, 160177.
- 9 P. C. Ray, Chem. Rev., 2010, **110**, 5332–5365.
- Z. A. ALOthman, D. Rodriguez-Padron, R. Luque and A. M.
   Balu, Curr. Opin. Green Sustain. Chem., 2021, 32, 100520.
- 11 Y. Zhang, J. Mei, C. Yan, T. Liao, J. Bell and Z. Sun, *Adv. Mater.*, 2020, **32**, 1902806.
- N. Baig, I. Kammakakam and W. Falath, *Mater. Adv.*, 2021,2, 1821–1871.
- Y. Chen, Z. Fan, Z. Zhang, W. Niu, C. Li, N. Yang, B. Chen andH. Zhang, *Chem. Rev.*, 2018, 118, 6409–6455.
- 14 X. Fu, J. Cai, X. Zhang, W. Di Li, H. Ge and Y. Hu, Adv. Drug Deliv. Rev., 2018, 132, 169–187.
- S. Witomska, T. Leydecker, A. Ciesielski and P. Samorì, *Adv. Funct. Mater.*, 2019, **29**, 1901126.

- 16 D. Wang, T. Xie and Y. Li, *Nano Res.*, 2009, **2**, 30–46.
- 17 E. Halvani Anaraki, A. Kermanpur, M. T. Mayer, L. Steier, T. Ahmed, S. H. Turren-Cruz, J. Seo, J. Luo, S. M. Zakeeruddin, W. R. Tress, T. Edvinsson, M. Grätzel, A. Hagfeldt and J. P. Correa-Baena, *ACS Energy Lett.*, 2018, **3**, 773–778.
- 18 M. Jeyaraj, S. Gurunathan, M. Qasim, M.-H. Kang and J.-H. Kim, *Nanomaterials*, 2019, **9**, 1719.
- S. Asokan, K. M. Krueger, V. L. Colvin and M. S. Wong, *Small*, 2007, 3, 1164–1169.
- 20 Z. Li and X. Peng, J. Am. Chem. Soc., 2011, **133**, 6578–6586.
- 21 R. Lesyuk, E. Klein, I. Yaremchuk and C. Klinke, *Nanoscale*, 2018, **10**, 20640–20651.
- 22 Y. Liu, G. Yuan, Z. Jiang, Z. Yao and M. Yue, *lonics (Kiel).*, 2015, **21**, 801–808.
- 23 T. D. Nguyen, *Nanoscale*, 2013, **5**, 9455–9482.
- Y. Xia, Y. Xiong, B. Lim and S. E. Skrabalak, .
- Y. Yang, X. Zhang, Y. Chen, X. Yang, J. Ma, J. Wang, L. Wang and W. Feng, ACS Appl. Mater. Interfaces, 2021, 13, 41102–41111.
- 26 H. Kaneko, T. Matsumoto, J. L. Cuya Huaman, M. Ishijima, K. Suzuki, H. Miyamura and J. Balachandran, *Inorg. Chem.*, 2021, **60**, 3025–3036.
- 27 S. J. Lee, Y. S. Son, J. H. Choi, S. S. Kim and S. Y. Park, *Catalysts*, 2021, **11**, 1–12.
- 28 R. Karimi-Chaleshtori, A. H. Nassajpour-Esfahani, M. R. Saeri, P. Rezai and A. Doostmohammadi, *Mater. Today Chem.*, 2021, **21**, 100496.
- P. Suchomel, L. Kvitek, R. Prucek, A. Panacek, A. Halder, S. Vajda and R. Zboril, *Sci. Rep.*, 2018, **8**, 1–11.
- M. B. Erande, M. S. Pawar and D. J. Late, ACS Appl. Mater. Interfaces, 2016, 8, 11548–11556.
- S. Zhu, Q. Liang, Y. Xu, H. Fu and X. Xiao, Eur. J. Inorg. Chem., 2020, 2020, 773–779.
- 32 B. Tian, B. Tian, B. Smith, M. C. Scott, Q. Lei, R. Hua, Y. Tian and Y. Liu, *Proc. Natl. Acad. Sci. U. S. A.*, 2018, **115**, 4345–4350.
- 33 Y. Yamada, M. Matsubara, A. Muramatsu, S. Takeda and K. Kanie, *Adv. Powder Technol.*, 2022, **33**, 103660.
- D. Zilevu and S. E. Creutz, *Chem. Mater.*, 2021, **33**, 5137–5146.
- 35 H. D. T. Duong, D. T. Nguyen and K. S. Kim, *Nanomaterials*, 2021, **11**, 1–17.
- 36 X. Li, X. Gao, W. Lu, H. Fouad, A. H. I. Mourad, M. Shaheer Akhtar and W. Guo, *Mater. Lett.*, 2022, **316**, 132056.
- 37 M. Heidariramsheh, M. M. Dabbagh, S. M. Mahdavi and A. Beitollahi, *Mater. Sci. Semicond. Process.*, 2021, **121**, 105401.

- 38 J. Xu, Q. Zhao, T. Hu, X. Chen and Y. Cao, *J. Nanoparticle Res.*, 2021, **23**, 1–10.
- 39 W. Zhao, M. Fang, F. Wu, H. Wu, L. Wang and G. Chen, J. Mater. Chem., 2010, 20, 5817–5819.
- A. Ejigu, B. Miller, I. A. Kinloch and R. A. W. Dryfe, *Carbon N. Y.*, 2018, **128**, 257–266.
- S. Majee, M. Song, S.-L. Zhang and Z.-B. Zhang, *Carbon N. Y.*, 2016, **102**, 51–57.
- 42 W. Qian, R. Hao, Y. Hou, Y. Tian, C. Shen, H. Gao and X. Liang, *Nano Res.*, 2009, **2**, 706–712.
- 43 C. E. Hamilton, J. R. Lomeda, Z. Sun, J. M. Tour and A. R. Barron, *Nano Lett.*, 2009, **9**, 3460–3462.
- D. Lee, B. Lee, K. H. Park, H. J. Ryu, S. Jeon and S. H. Hong, Nano Lett., 2015, 15, 1238–1244.
- 45 M. Ranjeh, F. Beshkar and M. Salavati-Niasari, *Compos. Part B Eng.*, 2019, **172**, 33–40.
- 46 M. Ranjeh, M. Ghiyasiyan-Arani, M. Slavati-Niasari and H. Moayedi, J. Mater. Res. Technol., 2020, 9, 2028–2036.
- J. Huang, X. Deng, H. Wan, F. Chen, Y. Lin, X. Xu, R. Ma and
   T. Sasaki, ACS Sustain. Chem. Eng., 2018, 6, 5227–5237.
- 48 L. Meng, S. Duwal, J. M. D. Lane, T. Ao, B. Stoltzfus, M. Knudson, C. Park, P. Chow, Y. Xiao, H. Fan and Y. Qin, *J. Am. Chem. Soc.*, 2021, **143**, 2688–2693.
- 49 J. F. Sánchez M., M. D. Sánchez, R. D. Falcone and H. A. Ritacco, *Phys. Chem. Chem. Phys.*, 2022, **24**, 1692–1701.
- 50 B. Wang, T. yan Chang, Z. Jiang, J. jia Wei and T. Fang, *Appl. Catal. B Environ.*, 2019, **251**, 261–272.
- 51 R. Guo, K. Zhang, Y. Liu, Y. He, C. Wu and M. Jin, *J. Mater. Chem. A*, 2021, **9**, 6196–6204.
- 52 R. Yadav, V. Kumar, V. Saxena, P. Singh and V. K. Singh, *Ceram. Int.*, 2019, **45**, 24999–25009.
- 53 C.-H. Choi, D.-H. Ko, H. Y. Jun, S. O. Ryu and D.-P. Kim, *Green Chem.*, 2020, **22**, 699–706.
- 54 C. H. Chang, B. K. Paul, V. T. Remcho, S. Atre and J. E. Hutchison, *J. Nanoparticle Res.*, 2008, **10**, 965–980.
- 55 G. M. Whitesides, *Nature*, 2006, **442**, 368–373.
- 56 K. S. Elvira, X. C. I Solvas, R. C. R. Wootton and A. J. Demello, *Nat. Chem.*, 2013, **5**, 905–915.
- V. V. K. Doddapaneni, J. A. Dhas, A. Chang, C. Choi, S. Han,
   B. K. Paul and C. Chang, MRS Energy Sustain., 2022, 9, 407–
- 58 G. N. Ahn, T. Yu, H. J. Lee, K. W. Gyak, J. H. Kang, D. You and D. P. Kim, *Lab Chip*, 2019, **19**, 3535–3542.
- 59 X. Z. Lin, A. D. Terepka and H. Yang, *Nano Lett.*, 2004, **4**, 2227–2232.
- S. Srikanth, S. Dudala, U. S. Jayapiriya, J. M. Mohan, S. Raut,
   S. K. Dubey, I. Ishii, A. Javed and S. Goel, *Sci. Rep.*, 2021, 11,
   1–12.
- 61 C.-H. Choi, Y. Kwak, R. Malhotra and C.-H. Chang, *Processes*, 2020, 8.
- P. G. Karagiannidis, S. A. Hodge, L. Lombardi, F. Tomarchio,
   N. Decorde, S. Milana, I. Goykhman, Y. Su, S. V Mesite, D.
   N. Johnstone, R. K. Leary, P. A. Midgley, N. M. Pugno, F.
   Torrisi and A. C. Ferrari, ACS Nano, 2017, 11, 2742–2755.
- 63 J. Shang, F. Xue and E. Ding, Chem. Commun., 2015, 51, 15811–15814.
- 64 C.-H. Choi, Y.-J. Park, X. Wu and D.-P. Kim, *Chem. Eng. J.*,

- 2018, **333**, 336–342.
- A. E. Del Rio Castillo, V. Pellegrini, A. Ansaldo, F. Ricciardella, H. Sun, L. Marasco, J. Buha, Z. Dang, L. Gagliani, E. Lago, N. Curreli, S. Gentiluomo, F. Palazon, M. Prato, R. Oropesa-Nuñez, P. S. Toth, E. Mantero, M. Crugliano, A. Gamucci, A. Tomadin, M. Polini and F. Bonaccorso, *Mater. Horizons*, 2018, 5, 890–904.
- X. Qiu, V. Bouchiat, D. Colombet and F. Ayela, *RSC Adv.*,2019, 9, 3232–3238.
- 67 S. Shoji and K. Kawai, in *MicroFluidics Technologies and Applications*, ed. B. Lin, Elsevier, 2011, pp. 1–25.
- 68 P. Zhu and L. Wang, *Lab Chip*, 2017, **17**, 34–75.
- 69 L. Lei, H. Zhang, D. J. Bergstrom, T. Anthony, K.-Y. Song and W. Zhang, *J. Micromechanics Microengineering*, 2020, **30**, 055001.
- 70 N. S. Satarkar, W. Zhang, R. E. Eitel and J. Z. Hilt, *Lab Chip*, 2009, **9**, 1773–1779.
- 71 L. Clime, D. Brassard, M. Geissler and T. Veres, *Lab Chip*, 2015, **15**, 2400–2411.
- 72 A. P. Washe, P. Lozano-Sánchez, D. Bejarano-Nosas, B. Teixeira-Dias and I. Katakis, *Microelectron. Eng.*, 2013, **111**, 416–420.
- 73 V. Hessel, H. Löwe and F. Schönfeld, *Chem. Eng. Sci.*, 2005, **60**, 2479–2501.
- 74 C. Wei, C. Yu, S. Li, F. Pan, T. Li, Z. Wang and J. Li, *Micromachines*, 2021, **12**, 901.
- 75 Y.-J. KO, S.-M. HA, H.-J. KIM, D.-H. LEE and Y. AHN, *J. Solid Mech. Mater. Eng.*, 2008, **2**, 445–454.
- 76 C. A. Cortes-Quiroz, A. Azarbadegan and E. Moeendarbary, World Acad. Sci. Eng. Technol., 2010, **61**, 170–175.
- 77 I. L. Ngo, T. K. Lai, H. J. Choi, H. T. T. Le, G. M. Kim and T. D. Dang, *Phys. Fluids*, 2020, **32**, 022004.
- 78 A. Venancio-Marques, F. Barbaud and D. Baigl, *J. Am. Chem. Soc.*, 2013, **135**, 3218–3223.
- 79 Z. Li, B. Zhang, D. Dang, X. Yang, W. Yang and W. Liang, Sensors Actuators A Phys., 2022, **344**, 113757.
- N.-T. Nguyen and Z. Wu, *J. Micromechanics Microengineering*, 2005, **15**, R1–R16.
- G. Yesiloz, M. S. Boybay and C. L. Ren, *Anal. Chem.*, 2017, 89, 1978–1984.
- 82 B. Sun, J. Jiang, N. Shi and W. Xu, *Process Saf. Prog.*, 2016, 35, 365–373.
- 83 V. Miralles, A. Huerre, F. Malloggi and M.-C. Jullien, *Diagnostics*, 2013, **3**, 33–67.
- D. Koziej, C. Floryan, R. A. Sperling, A. J. Ehrlicher, D. Issadore, R. Westervelt and D. A. Weitz, *Nanoscale*, 2013, **5**, 5468–5475.
- 85 T. Y. Chen, M. Baker-Fales and D. G. Vlachos, *Ind. Eng. Chem. Res.*, 2020, **59**, 10418–10427.
- A. J. L. Morgan, J. Naylon, S. Gooding, C. John, O. Squires, J. Lees, D. A. Barrow and A. Porch, *Sensors Actuators B Chem.*, 2013, **181**, 904–909.
- P. B. Kreider, K. J. Kim and C. H. Chang, RSC Adv., 2014, 4, 13827–13830.
- J. Marschewski, R. Brechbühler, S. Jung, P. Ruch, B. Michel and D. Poulikakos, *Int. J. Heat Mass Transf.*, 2016, **95**, 755–764.

- 89 L. Xu, J. Peng, C. Srinivasakannan, G. Chen and A. Q. Shen, *Appl. Surf. Sci.*, 2015, **355**, 1–6.
- L. Xu, J. Peng, C. Srinivasakannan, L. Zhang, D. Zhang, C. Liu,
   S. Wang and A. Q. Shen, *RSC Adv.*, 2014, 4, 25155–25159.
- 91 M. Shviro and D. Zitoun, *RSC Adv.*, 2013, **3**, 1380–1387.
- 92 L. Zhang, G. Niu, N. Lu, J. Wang, L. Tong, L. Wang, M. J. Kim and Y. Xia, *Nano Lett.*, 2014, 14, 6626–6631.
- 93 H. Yagyu, Y. Tanabe, S. Takano and M. Hamamoto, *Micro Nano Lett.*, 2017, **12**, 536–539.
- 94 M. V. Bandulasena, G. T. Vladisavljević and B. Benyahia, Chem. Eng. Sci., 2019, 195, 657–664.
- 95 S. Sharada, P. L. Suryawanshi, P. Rajesh Kumar, S. P. Gumfekar, T. B. Narsaiah and S. H. Sonawane, *Colloids Surfaces A Physicochem. Eng. Asp.*, 2016, **498**, 297–304.
- 96 L. Xu, C. Srinivasakannan, J. Peng, D. Zhang and G. Chen, Chem. Eng. Process. Process Intensif., 2015, 93, 44–49.
- 97 L. Xu, J. Peng, M. Yan, D. Zhang and A. Q. Shen, *Chem. Eng. Process. Process Intensif.*, 2016, **102**, 186–193.
- 98 C. H. Choi, E. Allan-Cole and C. H. Chang, *J. Mater. Chem. C*, 2015, **3**, 7262–7266.
- 99 C.-H. Choi, E. Allan-Cole and C. Chang, *CrystEngComm*, 2017, **19**, 1265–1272.
- 100 E. Chow, B. Raguse, E. Della Gaspera, S. J. Barrow, J. Hong, L. J. Hubble, R. Chai, J. S. Cooper and A. Sosa Pintos, *React. Chem. Eng.*, 2020, **5**, 356–366.
- L. Gomez, V. Sebastian, S. Irusta, A. Ibarra, M. Arruebo andJ. Santamaria, *Lab Chip*, 2014, 14, 325–332.
- H. Huang, H. Du Toit, S. Ben-Jaber, G. Wu, L. Panariello, N.
   T. K. Thanh, I. P. Parkin and A. Gavriilidis, *React. Chem. Eng.*, 2019, 4, 884–890.
- S. K. Lee, X. Liu, V. Sebastián Cabeza and K. F. Jensen, *Lab Chip*, 2012, **12**, 4080–4084.
- 104 M. Luty-Błocho, M. Wojnicki, K. Pacławski and K. Fitzner, Chem. Eng. J., 2013, 226, 46–51.
- 105 J. Ma and C. W. Li, Sensors Actuators, B Chem., 2018, 262, 236–244.
- G. Tofighi, A. Gaur, D. E. Doronkin, H. Lichtenberg, W.
  Wang, D. Wang, G. Rinke, A. Ewinger, R. Dittmeyer and J.
  D. Grunwaldt, J. Phys. Chem. C, 2018, 122, 1721–1731.
- 107 G. Tofighi, D. Degler, B. Junker, S. Müller, H. Lichtenberg, W. Wang, U. Weimar, N. Barsan and J. D. Grunwaldt, Sensors Actuators, B Chem., 2019, 292, 48–56.
- C. G. Yang, Z. R. Xu, A. P. Lee and J. H. Wang, *Lab Chip*, 2013, 13, 2815–2820.
- S. Lin, K. Lin, D. Lu and Z. Liu, *J. Environ. Chem. Eng.*, 2017,5, 303–309.
- 110 C. H. Choi, Y. W. Su and C. H. Chang, *CrystEngComm*, 2013, **15**. 3326–3333.
- N. Hao, Z. Xu, Y. Nie, C. Jin, A. B. Closson, M. Zhang and J. X.
   J. Zhang, *Chem. Eng. J.*, 2019, **378**, 122222.
- N. Hao, Y. Nie, Z. Xu, A. B. Closson, T. Usherwood and J. X.
   J. Zhang, *Chem. Eng. J.*, 2019, 366, 433–438.
- 113 N. Hao, Y. Nie and J. X. J. Zhang, *ACS Sustain. Chem. Eng.*, 2018, **6**, 1522–1526.
- 114 N. Hao, X. Chen, K. W. Jayawardana, B. Wu, M. Sundhoro and M. Yan, *Biomater. Sci.*, 2016, **4**, 87–91.
- N. Hao, Y. Nie and J. X. J. Zhang, *Microporous Mesoporous*

- Mater., 2018, **261**, 144-149.
- 116 R. Fan, X. Chen, Z. Wang, D. Custer and J. Wan, *Small*, 2017, 13, 1701154.
- 117 Y. He, K.-J. Kim and C.-H. Chang, *Nanotechnology*, 2017, **28**, 235602.
- W. Yang, H. Yang, W. Ding, B. Zhang, L. Zhang, L. Wang, M. Yu and Q. Zhang, *Ultrason. Sonochem.*, 2016, 33, 106–117.
- J. Wang, H. Zhao, Y. Zhu and Y. Song, J. Phys. Chem. C,2017, 121, 3567–3572.
- 120 Z. H. Tian, J. H. Xu, Y. J. Wang and G. S. Luo, *Chem. Eng. J.*, 2016, **285**, 20–26.
- J. Pan, A. O. El-Ballouli, L. Rollny, O. Voznyy, V. M. Burlakov, A. Goriely, E. H. Sargent and O. M. Bakr, ACS Nano, 2013, 7, 10158–10166.
- H. Y. Jun, C. H. Chang, K. S. Ahn, S. O. Ryu and C. H. Choi, *CrystEngComm*, 2020, **22**, 646–653.
- M. Marelli, F. Bossola, G. Spinetti, E. Sangalli, V. D. Santo, R. Psaro and L. Polito, ACS Appl. Mater. Interfaces, 2020, 12. 38522–38529.
- 124 X. Zhu, Q. Zhang, Y. Li and H. Wang, J. Mater. Chem., 2010, 20, 1766–1771.
- D. Che, X. Zhu, P. Liu, Y. Duan, H. Wang, Q. Zhang and Y. Li, *J. Lumin.*, 2014, **153**, 369–374.
- 126 Y. He, Z. Chen and C. Chang, *Nanotechnology*, 2020, **31**, 235603.
- 127 G. Doria, J. Conde, B. Veigas, L. Giestas, C. Almeida, M. Assunção, J. Rosa and P. V. Baptista, *Sensors*, 2012, **12**, 1657–1687.
- 128 C. N. R. Rao, G. U. Kulkarni, P. J. Thomas and P. P. Edwards, *Chem. Soc. Rev.*, 2000, **29**, 27–35.
- 129 H. W. Tan, J. An, C. K. Chua and T. Tran, *Adv. Electron. Mater.*, 2019, **5**, 1800831.
- E. Sánchez-López, D. Gomes, G. Esteruelas, L. Bonilla, A. L. Lopez-Machado, R. Galindo, A. Cano, M. Espina, M. Ettcheto, A. Camins, A. M. Silva, A. Durazzo, A. Santini, M. L. Garcia and E. B. Souto, *Nanomaterials*, 2020, 10, 292.
- 131 V. Sebastian, C. D. Smith and K. F. Jensen, *Nanoscale*, 2016,8, 7534–7543.
- M. Kandasamy, S. Sahoo, S. K. Nayak, B. Chakraborty and C.S. Rout, *J. Mater. Chem. A*, 2021, 9, 17643–17700.
- 133 X. Zheng and L. Zhang, *Energy Environ. Sci.*, 2016, **9**, 2511–2532.
- D. Nunes, A. Pimentel, A. Gonçalves, S. Pereira, R. Branquinho, P. Barquinha, E. Fortunato and R. Martins, *Semicond. Sci. Technol.*, 2019, **34**, 043001.
- T. Guo, M. S. Yao, Y. H. Lin and C. W. Nan, *CrystEngComm*, 2015, **17**, 3551–3585.
- 136 C.-H. Choi and C. Chang, *Cryst. Growth Des.*, 2014, **14**, 4759–4767.
- 137 Y. Zhang, Q. Zhou, J. Zhu, Q. Yan, S. X. Dou and W. Sun, Adv. Funct. Mater., 2017, 27, 1702317.
- 138 N. Mishra, V. G. Vasavi Dutt and M. P. Arciniegas, *Chem. Mater.*, 2019, **31**, 9216–9242.
- J. N. Freitas, A. S. Gonçalves and A. F. Nogueira, *Nanoscale*, 2014, 6, 6371–6397.
- 140 B. K. H. Yen, N. E. Stott, K. F. Jensen and M. G. Bawendi, Adv. Mater., 2003, 15, 1858–1862.

- 141 H. Nakamura, Y. Yamaguchi, M. Miyazaki, H. Maeda, M. Uehara and P. Mulvaney, *Chem. Commun.*, 2002, **23**, 2844–2845.
- H. Nakamura, A. Tashiro, Y. Yamaguchi, M. Miyazaki, T. Watari, H. Shimizu and H. Maeda, Lab Chip, 2004, 4, 237–240
- 143 K.-J. Kim, R. P. Oleksak, C. Pan, M. W. Knapp, P. B. Kreider, G. S. Herman and C.-H. Chang, RSC Adv., 2014, 4, 16418– 16424
- M. Sen, in *Nanotechnology and the Environment*, ed. M. Sen, IntechOpen, Rijeka, 2020, p. Ch. 6.
- 145 K. S. Novoselov, A. Mishchenko, A. Carvalho and A. H. Castro Neto, *Science* (80-. )., 2016, **353**, aac9439.
- 146 L. Shi and T. Zhao, *J. Mater. Chem. A*, 2017, **5**, 3735–3758.
- 147 P. Miró, M. Audiffred and T. Heine, *Chem. Soc. Rev.*, 2014,43, 6537–6554.
- 148 M. Lotya, P. J. King, U. Khan, S. De and J. N. Coleman, ACS Nano, 2010, 4, 3155–3162.
- T. J. Nacken, C. Damm, J. Walter, A. Rüger and W. Peukert, *RSC Adv.*, 2015, **5**, 57328–57338.
- 150 K. R. Paton, J. Anderson, A. J. Pollard and T. Sainsbury, Mater. Res. Express, 2017, 4, 25604.
- 151 C.-H. Choi, D.-H. Ko, B. Park, Y. Choi, W. Choi and D.-P. Kim, *Chem. Eng. J.*, 2019, **358**, 1594–1600.
- H. Ahmed, A. R. Rezk, B. J. Carey, Y. Wang, M. Mohiuddin, K. J. Berean, S. P. Russo, K. Kalantar-zadeh and L. Y. Yeo, Adv. Mater., 2018, 30, 1704756.
- M. Buzaglo, M. Shtein and O. Regev, *Chem. Mater.*, 2016,
   28, 21–24.
- 154 Y.-Z. Wang, T. Chen, X.-F. Gao, H.-H. Liu and X.-X. Zhang, *Mater. Express*, 7, 491–499.
- H. Yurdakul, Y. Göncü, O. Durukan, A. Akay, A. T. Seyhan, N. Ay and S. Turan, Ceram. Int., 2012, 38, 2187–2193.
- 156 A. T. Seyhan, Y. Göncü, O. Durukan, A. Akay and N. Ay, *J. Solid State Chem.*, 2017, **249**, 98–107.
- 157 E. Ilhan-Ayisigi, B. Yaldiz, G. Bor, A. Yaghmur and O. Yesil-Celiktas, *Colloids Surfaces B Biointerfaces*, 2021, **201**, 111633.
- 158 Y. Sun and Y. Ren, *Part. Part. Syst. Charact.*, 2013, **30**, 399–
- 159 L. Fang, S. Seifert, R. E. Winans and T. Li, *Small*, 2022, **18**, 2106017.
- A. Ghazal, M. Gontsarik, J. P. Kutter, J. P. Lafleur, D. Ahmadvand, A. Labrador, S. Salentinig and A. Yaghmur, *J. Phys. Chem. Lett.*, 2017, **8**, 73–79.